THE TRANSACTIONS OF

The Royal Institution of Naval Architects

Vol 159 Part B2 2017

International Journal of Small Craft Technology

The Transactions of The Royal Institution of Naval Architects – Part B

International Journal of Small Craft Technology

ISSN 1740-0694 (Print)
ISSN 1740-2719 (CD-ROM)
ISSN 1740-0708 (Online)

The **International Journal of Small Craft Technology (IJSCT)** provides a forum for the reporting and discussion on technical and scientific issues associated with research and development of recreational and commercial small craft. The IJSCT is published as Part B of the Transactions of The Royal Institution of Naval Architects. Contributions in the form of scientific and technical papers and notes on the following aspects of small craft technology are invited:

- Design (including design methodologies, design practice, innovative concepts, design analysis tools, series data from experiments, design for safety, computer aided design).
- Construction (including one-off construction and series production issues, facility design, materials, joining technologies, reconstructions and rebuilds of historic craft).
- Operation (including racing, short handed sailing, equipment, results of seatrials, results of instrumentation, gear failure, human or vessel casualties, low technology operations).
- Regulation (including international, national, and regional regulatory frameworks, classification, codes of practice, rating rules).

PAPERS

Papers may introduce new theory or evaluate existing theory, or describe experimental or novel practical work, Papers presenting case histories will report on new or existing techniques, including design and production. Papers may also provide literary reviews which appraise and evaluate published work. All papers are refereed.

TECHNICAL NOTES

Technical notes will provide early announcement of new ideas, findings, procedures, applications, interim results, etc., which might later on form part of a full paper. Technical notes are refereed as for papers, but due allowance will be made for their immediate nature.

DISCUSSION

Comments on papers and technical notes will normally be published in the first available issue of the IJME following that in which the paper was published.Discussion may be continued in subsequent issues, at the discretion of the Editor. Authors will be invited to respond to published comment.

The Transactions of The Royal Institution of Naval Architects

Vol 159 Part B2 2017 **ISSN 1740 – 0694**

International Journal of Small Craft Technology

CONTENTS

PAPERS

TECHNICAL NOTES

There are no Technical Notes published in this issue of the IJSCT

DISCUSSION

There are no Discussions published in this issue of the IJSCT

FLYING SHAPE PREDICTION OF ASYMMETRIC SPINNAKERS – AN EXPERIMENTAL DATA SET FOR VALIDATION OF FSI-SIMULATIONS

(DOI No: 10.3940/rina.ijsct.2017.b2.199)

H F Renzsch, Delft University of Technology, the Netherlands and **K U Graf**, University of Applied Sciences Kiel, Germany

SUMMARY

In this paper the results of wind tunnel tests on two different asymmetric spinnakers are presented. During these tests forces and flying shapes at different apparent wind angles and trims were recorded by 6DoF balance and photogrammetry. As these tests are intended as a validation benchmark for FSI-simulations on downwind sails, the sail moulds, incident flow data as well as measured forces and flying shapes are available from the authors' website.

NOMENCLATURE

AWA	Apparent wind angle [°]
AWS	Apparent wind speed [m/s]
A_x	Driving force area [-]
A_y	Side force area [-]
c_D	Drag coefficient [-]
c_L	Lift coefficient [-]
E*t	Young's modulus times thickness [N/m]
tMax	Location of max. draft, normalised by girth [%]
V_x	Heeling moment volume [-]
V_z	Yawing moment volume [-]
AMG	Mid girth asymmetric spinnaker [m]
ASF	Foot length asymmetric spinnaker [m]
ASL	Longest leech asymmetric spinnaker [m]
FSI	Fluid-Structure-Interaction
ISP	Height of spinnaker halyard exit above deck [m]
J	Foot length of headsail triangle [m]
TPS	Tackline exit in front of mast [m]

1. INTRODUCTION

In recent years, various parties have proposed an increasing number of Fluid-Structure-Interaction (FSI) simulation methods and some are, actually, already in industrial use. Yet, neither publically available validation data, nor any rigorous code validations have been published. To ensure customer confidence, basically it is a requirement for any kind of simulation usage (= approximation of a physical reality by mathematical model), to prove the accuracy of this simulation by reproducible comparison to experimental data.

In general aerospace or naval architectural practice a range of generally well accepted validation cases is available to check and ensure correctness of simulation results like the AGARD 445.6 wing (Yates & Carson, 1987) , the Moeri (Kriso) Container Ship (Hino, 2005) or the *Sailing Yacht Reseach Foundation's* Wide-Light study (Claughton, 2015).

Looking specifically at downwind sails, during recent years, a huge amount of significant experimental data on the relevant aerodynamics has been published, significantly furthering the understanding of the flow around the sail and confidence in wind tunnel testing. Data relevant to the validation of the simulation of flow around downwind sails has, for example, been published by Bot *et al.* (Bot *et al*, 2014) and associated papers. Within this project, forces and pressure distribution were measured on a soft sail, as well as pressure distribution on a rigid model of the measured flying shape of the soft sail. The rigid geometry as well as measurement results for soft and rigid sail are published, providing a complete set of validation data for CFD simulations. Unfortunately the moulded shape of the sail as well as structural information are not available, preventing the use of the case for the validation of FSI-simulations.

Validation of the structural code is still mostly limited to the classical experiments on e.g. pressurised tubes by (Stein & Hedgepeth, 1961), or experiments on airbag or parachute opening (e.g. Shortis *et al*, 2007, Pruett *et al*, 2009 or Chae *et al*, 2009), having little semblance to a sail. To the author's knowledge, no publicised experimental data on the behaviour of a sail-like (highly flexible, tensioned by pressure differential) structure in viscous flow is available.

Against this background, the intent of this project is to provide a data set for validation of downwind sail FSI simulations by providing moulded as well as flying shapes and force measurements. This data set comprises the moulded and flying shapes as CAD files, and spreadsheets with measured forces and moments, sail trimming information, sail structural information and incident flow conditions.

2. METHODOLOGY

2.1 WIND TUNNEL

The experiments for the data set were conducted at the Yacht Research Unit Kiel's (YRU-Kiel) Twisted Flow Wind Tunnel (TFWT) (Graf & Müller, 2005). The general layout of this open-jet wind tunnel is depicted in Figure 1. The outlet of the boundary layer section has a cross section of 3.60 x 2.40 m (B x H), the centre of the turntable is 2.17 m away from this outlet. Forces are measured in a model-fixed coordinate system by a six-component balance mounted below the wind tunnel floor and fully decoupled from any ambient vibration.

Attached to the balance is the yacht model consisting of hull, deck with fittings, rig and sails. The wind tunnel floor is entirely separate from the balance. Transfer of forces from floor to model is prevented by a small gap of approximately 3mm in between. Due to the stiffness of the balance this gap is stable over the entire range of measurable forces.

The vertical velocity gradient of the twisted flow is created by using blockage elements within the boundary layer section. Eddies created by these blockage elements are broken up by screens mounted downstream (see Figure 2).

Vanes mounted at the outlet of the boundary layer section manipulate the flow direction. Their position is controlled by pre-tensioned cross-wires (see Figure 3).

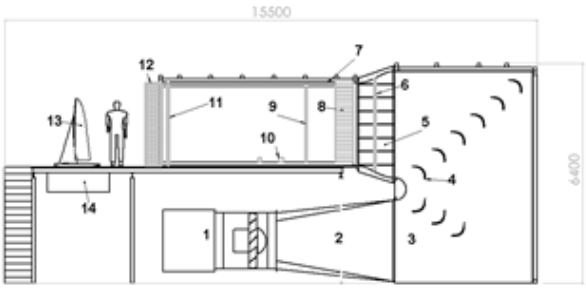

Figure 1: General layout of YRU-Kiel wind tunnel

Components of wind tunnel (Figure 1):

1: Inlet muffler
2: Diffusor
3: Settling chamber
4: Turning vanes
5: Contraction
6: Mesh screen
7: Boundary layer section
8: Flow straightener
9: Mesh screen
10: Blockage elements
11: Mesh screen
12: Twist flow vanes
13: Yacht model
14: Balance

Figure 2: Blockage elements and mesh screens with spires

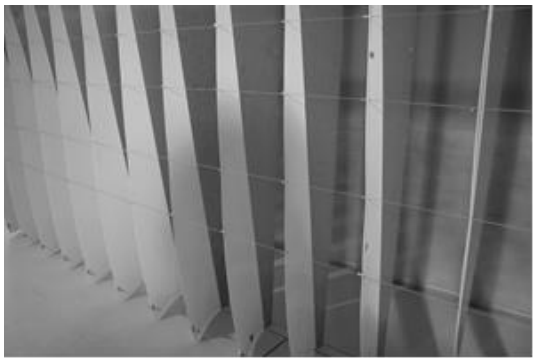

Figure 3: Twist flow vanes with control wires

Wind speed is measured by two Constant Temperature Anemometers (CTAs), one at the outlet of the boundary layer section, one right in front of the model, slightly above masthead height (position is indicated in CAD files). Both CTAs are regularly calibrated. Force areas during measurement and for evaluation are calculated using the velocity measured at the latter position to account for varying blockage effects due to changing model position and sail trim.

Air temperature is measured at the outlet of the boundary layer section and converted to density by a lookup table included in the data recording system.

Longer term flow measurements by constant temperature anemometer at 4kHz sampling frequency have indicated a turbulence level of 0.26% with most of the turbulence concentrated at low frequencies (below 100 Hz).

Calibration of the balance indicates an accuracy of force and moment measurements of about 2%.

2.2 PHOTOGRAMMETRY

Flying shape measurements are taken by means of photogrammetry (Müller & Graf, 2009). To capture instantaneous shapes of the usually unsteady sail four cameras are mounted downwind of the model and triggered simultaneously. The sails, the model and the wind tunnel floor are fitted with coded targets, allowing fast and reliable processing of the points locations in space. Evaluation of the photos is done using the software PhotoModeller Pro 6.4.0.821 by Eos Systems Inc., Canada.

Typically a downwind sail is fitted with about 60 coded targets on the surface plus about 30 non-coded marks along the leeches and at the corners, allowing accurate capturing of the shape. Nevertheless, it has to be kept in mind that small geometrical details like corner wrinkles (see Figure 4) are not captured by this method. Further, as only the locations of the marks are known, any surface fitted to the will only be an approximation in-between these marks. On the upside, this measurement technique allows to capture instantaneous shapes of a moving geometry, opposed to e.g. laser scanning.

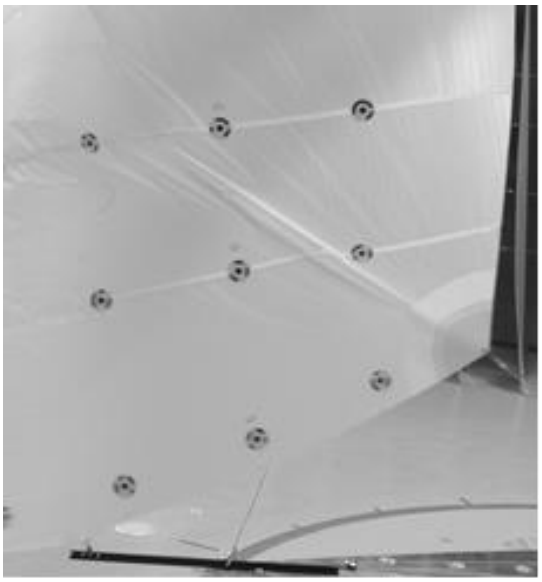

Figure 4: Corner wrinkle detail not captured by photogrammetry

To allow accurate measurements, all four cameras used in the measurements were calibrated using as wind tunnel model-sized calibration sheet for all used focal length.

According to product literature an accuracy of 0.02% of object size is achievable by sub-pixel marking of coded or circular targets. For the wind tunnel model this would correspond to 0.04mm. Validation tests on wind tunnel model sized bodies of known shape indicate a measurement accuracy of about 1 mm at the worst areas of a photo (near the edges) using hand set marks can safely be achieved.

Measurement accuracy for points on a fast moving object (relative to exposure time) cannot be exactly quantified. The points appear blurred on the photos, the software detects the location with the strongest contrast to the surrounding, respectively where the target spent the most time during camera sensor exposure. To provide a measure for accuracy and magnitude of motion, at least three individually measured geometries of each state are given in the CAD files.

2.3 MEASUREMENT PROCEDURE

For the measurement of forces and flying shape for a given *AWA* the sails are trimmed for maximum driving force, disregarding heeling moment. During the trimming process care is taken to achieve a standard deviation of forces and moments below 2% at the chosen trim. Once an optimum trim is found and forces have stabilised, these forces are recorded as an average over 5 seconds. Following that, three or more sets of photos of the sails are taken in short succession. By using several sets of photos, it is intended to capture the range of dynamic motion of the sail due to dynamic effects like periodic flow separation.

3. EXPERIMENTAL SETUP

3.1 FLOW CONDITIONING

Flow conditions in the twisted flow wind tunnel are designed to mimic the incident flow on as can be observed on a yacht moving downwind. Due to the combination of height dependent True Wind Speed (*TWS*) and boat speed a vertical gradient of Apparent Wind Speed (*AWS*) and Angle (*AWA*) results, the twisted flow. To achieve this vertical gradient the incident flow is slowed down in the lower regions by blockage elements within the boundary layer section and deflected by vanes at the outlet.

Ideally, the incident flow would conform to a vectorial superposition of the hypothetic boat speed and the logarithmic atmospheric wind profile given by

$$TWS(z) = TWS_{10m}\left(\frac{z}{10m}\right)^{e}$$

with *e* being in the range of 0.1 to 0.17.

Figure 5 gives the velocity and twist profile as measured at the centre of the turn table. All measurements were taken at a wind speed of 5.0 m/s measured at a height of 1.78m above floor.

Further details will be available from the measurement protocols.

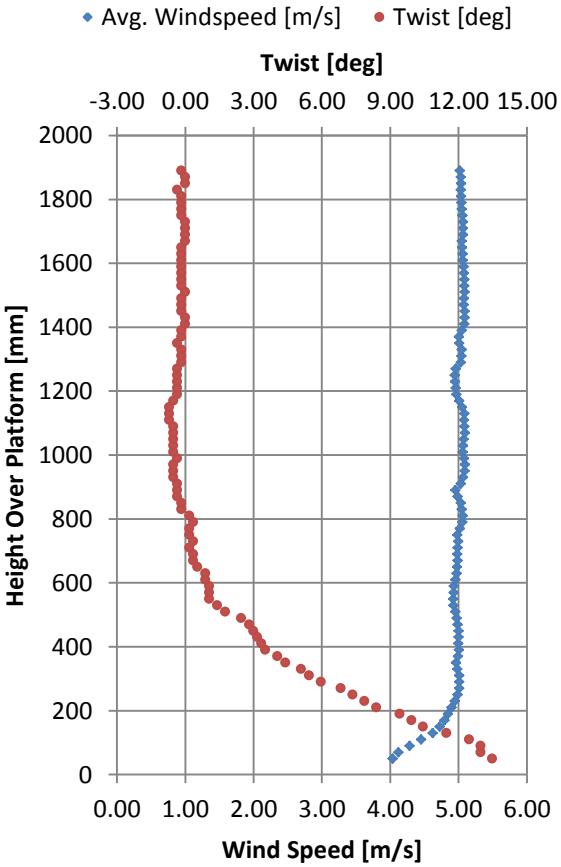

Figure 5: Velocity and twist profile at wind tunnel model

3.2 SAIL DESIGNS & YACHT MODEL

For the purpose of this study two asymmetric spinnaker designs for different optimum *AWA*s were created. Sail design "A" resembles a narrow cut spinnaker as carried on a fast planning boat like a skiff, while sail design "B" is significantly wider shouldered, resembling a more conventional yacht spinnaker. Geometric data on the sail designs is given in Table 1. While sail "B" has just 8% more measured sail area, its geometric area is a whopping 20% larger. This is due to the area distribution, pushing area into the unmeasured ¼ and ¾ girths. This is corroborated by the difference in luff and leech round, both being larger by about 10 percentage points on sail "B". Interestingly, sail "B" is of significantly flatter section design. An impression of the difference between the designs is given in Figures 6 and 7.

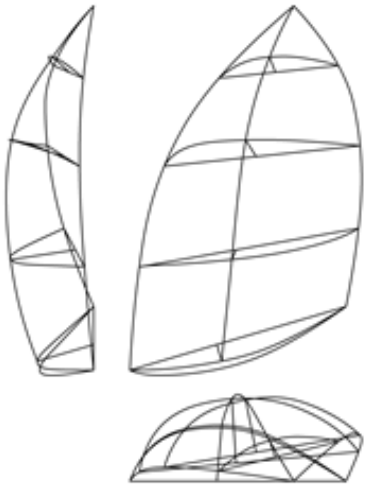

Figure 6: Impression of spinnaker "A"

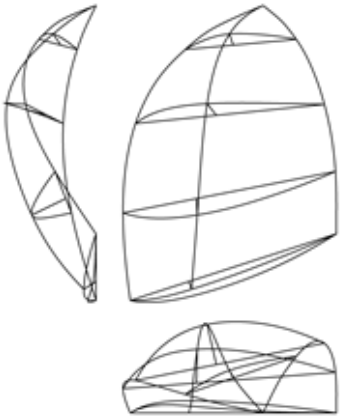

Figure 7: Impression of spinnaker "B"

The sails were fitted on the YRU-Kiel's generic yacht model resembling a 40' cruiser-racer. The spinnakers head and tack were fixed in place without adjustable halyard or tack line. As the scope of the study is limited to the spinnakers a readily available mainsail was used.

Based on the designed shape panels were developed for both sails in a cross-cut pattern. Assuming new spinnaker cloth to be strong enough to take the diagonal stresses near the corners it was decided to forgo tri-radial panelling to reduce the risk of manufacturing inaccuracies. The panelling is shown in Figure 8. During the tests it turned out to be necessary to strengthen the luff of spinnaker "A" by a 1cm wide strip of insignia sailcloth (180g/m²) to prevent the glued seams from opening up. The material properties of the spinnaker cloth are given in Table 2. The fill axis is parallel to the upper panel edges. As sheet 140 kg breakload Dyneema® kite line was used.

Moulds and panellisation of both spinnakers as well as geometry of the wind tunnel model are given in the CAD files.

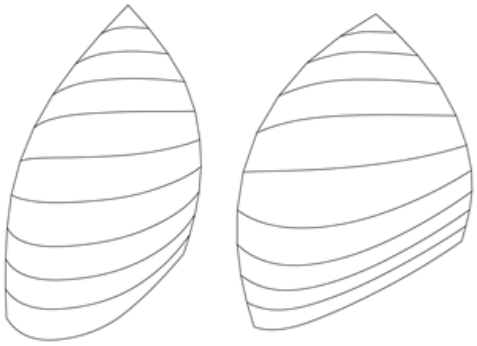

Figure 8: Panelling of sails

3.3 TEST MATRIX

Forces and moments were measured for both sail sets at 3.75° steps ranging from *AWA* 60° to 142.5° for sail set "A" and 78.75° to 150° for sail set "B".

Images for photogrammetric evaluation were taken at *AWA*s 75°, 90° and 105° for sail set "A" and 90°, 105° and 120° for sail set "B".

4. RESULTS

4.1 FORCES & MOMENTS

For comparison purposes driving and side forces as well as heeling and yawing moments are given as force areas respectively moment volumes, removing the influence of slight *AWS* variations and air temperature, respectively density variations. These are calculated by

$$ForceArea = \frac{Force}{0.5 \cdot \rho \cdot u^2}$$

respectively

$$MomentVolume = \frac{Moment}{0.5 \cdot \rho \cdot u^2} \cdot$$

No windage correction is applied to the resulting forces and moments as any approach based either on calculated windage of hull, mast and stays or measured without sails is deemed to be too questionable for comparison to CFD as interaction effects are neglected.

The resulting force areas and moment volumes are given in Figures 9 and 10. From Figure 9 it is evident that sail set "B" is able to generate about 10% more driving force than sail set "A", albeit at the cost of a smaller usable wind range. During the wind tunnel tests it was not possible to achieve *AWA*s smaller than 78.75° at which, incidentally, the crossover with sail set "A" approximately occurs. Lift and drag coefficients based on measured sail area (A_{Main} = 0.483m²) are given in Figure 11. Even though the differences in force areas are somewhat negated by the difference in size for the coefficient calculation, the larger spinnaker (sail set "B") is still more effective as well as more efficient at *AWA*s between 90° and 120°.

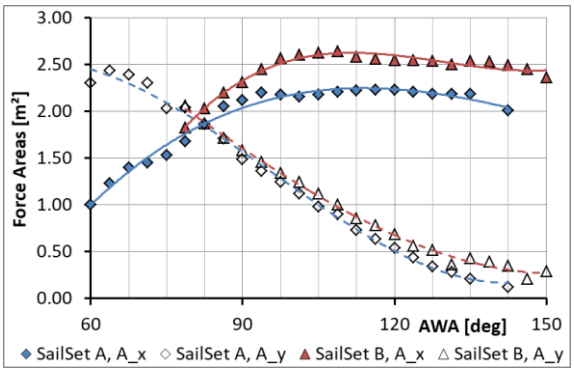

Figure 9: Driving (A_x) and side (A_y) force areas for sail sets at optimum trim

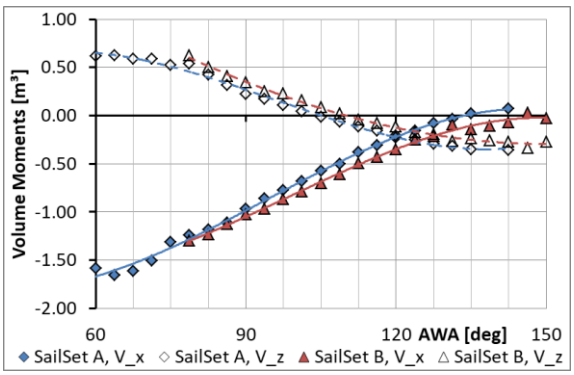

Figure 10: Heeling (V_x) and yawing (V_z) moment volumes for sail sets at optimum trim

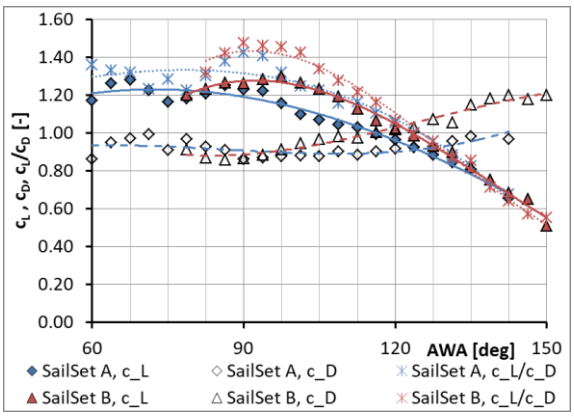

Figure 11: Lift (c_L) and drag (c_D) coefficients, aerodynamic efficiency c_L/c_D

All measured results are available as tabular data.

4.2 PHOTOGRAMMETRY

An exemplary result from the photogrammetric analysis is given in Figures 12 an 13. In Figure 12 the recognised coded targets (circular) as well as the hand detected edge locations (crosses) are well evident. In Figure 13 the setting of the cameras around the sail is depicted. For optimum accuracy it would be best to have any point on three individual photos with view axes at right angles. Unfortunately this is not possible on a highly curved shape like a sail. Therefore care has been taken to ensure that every marker is present on at least two photos with four cameras distributed in reference to the sails curvature, horizontally as well as vertically. Accordingly the cameras are placed on basically three horizontal and two vertical axes.

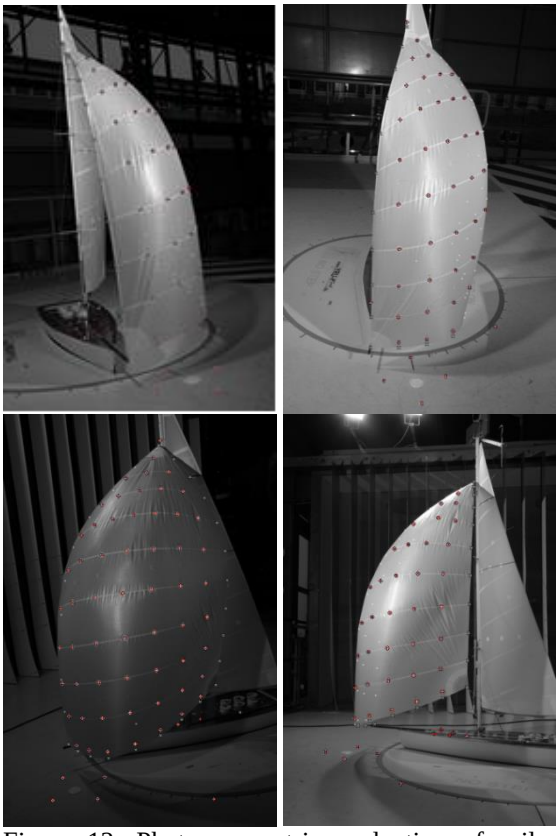

Figure 12: Photogrammetric evaluation of sail shape: processed photo set

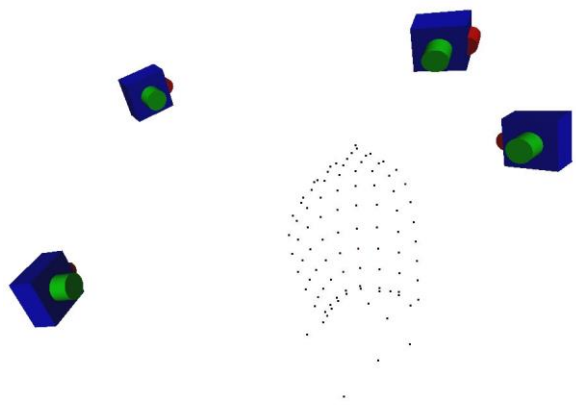

Figure 13: Camera orientation around sail

4.3 FLYING SHAPES

The point clouds resulting from photogrammetric evaluation were scaled and oriented to the CAD model of the wind tunnel model. The panel edges (seams) and the sail's surface were reconstructed from the point cloud. Exemplary results for both sail sets are given in Figures 14 to 19.

Both Figures give an idea of the dynamics of the sail. On spinnaker "A" (Figure 14) the motion occurs mostly at the luff with one case deviating from the other two. Basically this is a slight curling / flapping motion alternating between the lower and the upper luff. On spinnaker "B" the motion appears to occur in the whole sail. As indicated by Figure 15 the luff has a similar motion as for spinnaker "A", additionally the motion seems to be carried into the body of the sail until the leech.
In the CAD files the measured points as well as the reconstructed flying shapes of spinnaker and main are given. Further the files contain the individual lead positions and sheet lengths at the various trimming states. At no point during the measurements was the spinnaker sheet deflected by the main boom.

5. DATA SET

A data set containing the geometries as designed (yacht model, as well as the sails' moulded shapes), the measured flying shapes and tabular data on incident flow conditions and measured forces / moments is available from the authors' website. It can be downloaded at http://fluidengineeringsolutions.com/downwindsailvalidationdata/ .

6. CONCLUSIONS

In this paper a comprehensive wind tunnel investigation of two different spinnakers has been presented as validation testcase for FSI-simulations. A data package consisting of CAD data of the wind tunnel model, designed shapes and flying shapes as well as tabular data on incident flow conditions and measurement results is available from the authors' website. Any questions, suggestions or critique that enables us to improve the study and the available data sets are greatly appreciated. Please direct any enquiries to hannes @fluidengsol.com.

7. ACKNOWLEDGEMENTS

A big Thank You has to go to the Yacht Research Unit Kiel and in particular to Prof. Graf for making this study possible by providing wind tunnel time and personnel, software licenses and funding for the manufacturing of the tested sails.

8. REFERENCES

1. BOT, P., VIOLA, I.M., FLAY, R.G.J., BRETT, J.-S. (2014) Wind-tunnel pressure measurements on model-scale rigid downwind sails. Ocean Engineering, 90, 84. DOI: 10.1016/j.oceaneng.2014.07.024
2. CHAE D. B., HA W. P., KIM J. H., LEE J. H. and LEE J. K. (2009) *Validation Methodology on Airbag Deployment Process of Driver Side Airbag* 21st International Technical Conference on the Enhanced Safety of Vehicles, Stuttgart, Germany
3. CLAUGHTON, A. R. (2015) *SYRF Wide-Light Project* Sailing Yacht Research Foundation, http://sailyachtresearch.org/19-library/47-Wide-Light (accessed 14th August 2016)
4. GRAF, K. and MÜLLER, O. (2005) *Der Twist-Flow-Windkanal der Yacht Research Unit Kiel* 25th Symposium Yacht Design and Yacht Construction, Hamburg, Germany
5. HINO, T. (ed) (2005) *Proceedings of CFD Workshop Tokyo 2005* NMRI report, Tokyo, Japan
6. LASHER, W. C. (2003) *Experimental Force Coefficients for a Parametric Series of Spinnakers* 16th Chesapeake Sailing Yacht Symposium, Annapolis, MD
7. MÜLLER, O. and GRAF, K. (2009) *Photogrammetric Investigation of the Flying Shape of Spinnakers in a Twisted Flow Wind Tunnel* 19th Chesapeake Sailing Yacht Symposium, Annapolis, MD
8. PRUETT, M., ACCORSI, M. and CHARLES, R. D. (2009) *Validation of Computational Structural Dynamics Models for Parachute Systems* 20th AIAA Aerodynamic Decelerator Systems Technology Conference and Seminar, Seattle, WA
9. SHORTIS, M. R., ROBSON, S., JONES, T. W. and LUNSFORD, C. B. (2007) *Parachute model validation using image sequences* Eighth Conference on Optical 3-D Measurement Techniques, Zurich, Switzerland
10. STEIN, M. and HEDGEPETH, J. M. (1961) *Analysis of Partly Wrinkled Membranes* NASA
11. VIOLA, I. M. and FLAY, R. G. J. (2010) *Pressure Distribution on Modern Asymmetric Spinnakers* International Journal of Small Craft Technology, Trans. RINA, Vol. 152 Part B1, pp.41 – 50, DOI: 10.3940/rina.ijsct.2010.b1.103
12. YATES, E. and CARSON, J. R. (1987) *AGARD standard aeroelastic configurations for dynamic response. Candidate configuration I.-wing 445.6* NASA Technical Documents

APPENDICES

Table 1: Spinnaker measurements

		Spinnaker "A"	Spinnaker "B"
Luff	[m]	1.675	1.813
Leech	[m]	1.361	1.480
Luff Round	[%]	13.5	23.3
Leech Round	[%]	20.9	32.2
Mitre	[m]	1.583	1.712
Foot	[m]	1.067	1.093
Foot Girth	[m]	1.064	1.086
1/4 Girth	[m]	1.105	1.165
1/2 Girth	[m]	0.965	0.953
3/4 Girth	[m]	0.538	0.600
Foot Chord	[m]	0.899	1.067
1/4 Chord	[m]	0.892	1.069
1/2 Chord	[m]	0.796	0.953
3/4 Chord	[m]	0.493	0.580
Foot Depth	[%]	26.1	6.7
1/4 Depth	[%]	29.4	17.4
1/2 Depth	[%]	28.1	22.2
3/4 Depth	[%]	18.9	11.9
Foot tMax	[%]	40.3	28.5
1/4 tMax	[%]	44.2	34.7
1/2 tMax	[%]	47.0	42.8
3/4 tMax	[%]	47.3	43.1
1/4 twist	[°]	5.37	4.43
1/2 twist	[°]	9.37	11.25
3/4 twist	[°]	13.91	18.99
Area Geom.	[m²]	1.278	1.525
ISP	[m]	1.465	1.465
J	[m]	0.460	0.460
TPS	[m]	0.653	0.653
ASL	[m]	1.518	1.647
ASF	[m]	1.067	1.093
AMG	[m]	0.965	0.953
Area Meas.	[m²]	1.247	1.346

Table 2: Material properties of spinnaker cloth (Contender SK75®)

Weight	[g/m²]	41
E*t Warp	[N/m]	1.18E+05
E*t Fill	[N/m]	6.60E+04
E*t Bias	[N/m]	5.63E+04

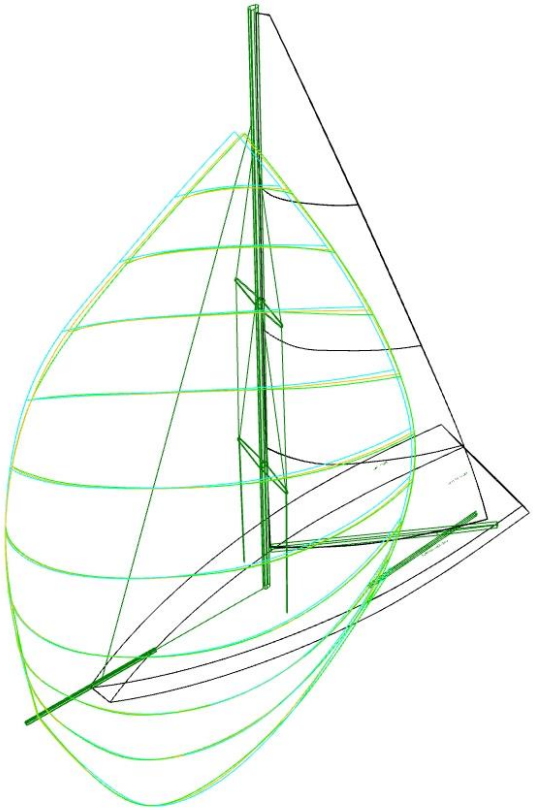

Figure 14: Sail set “A” at an AWA of 75°, three consecutive sets of photos

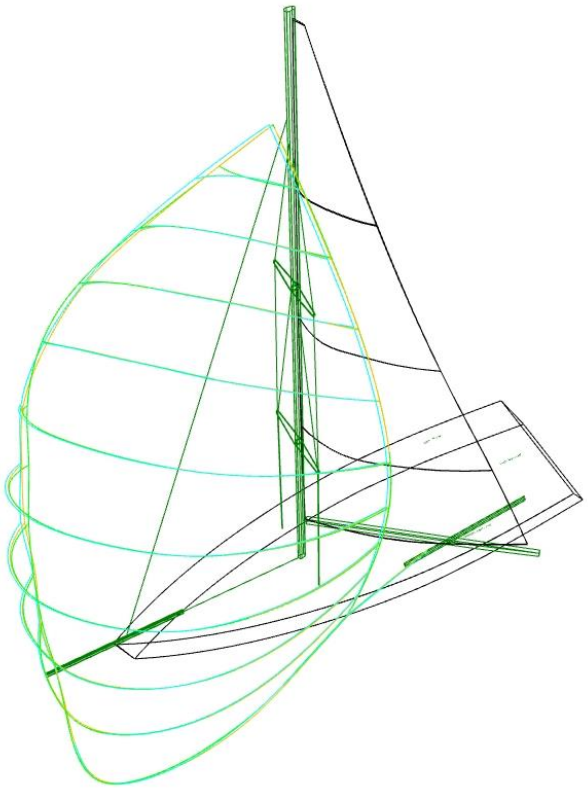

Figure 15: Sail set “A” at an AWA of 90°, three consecutive sets of photos

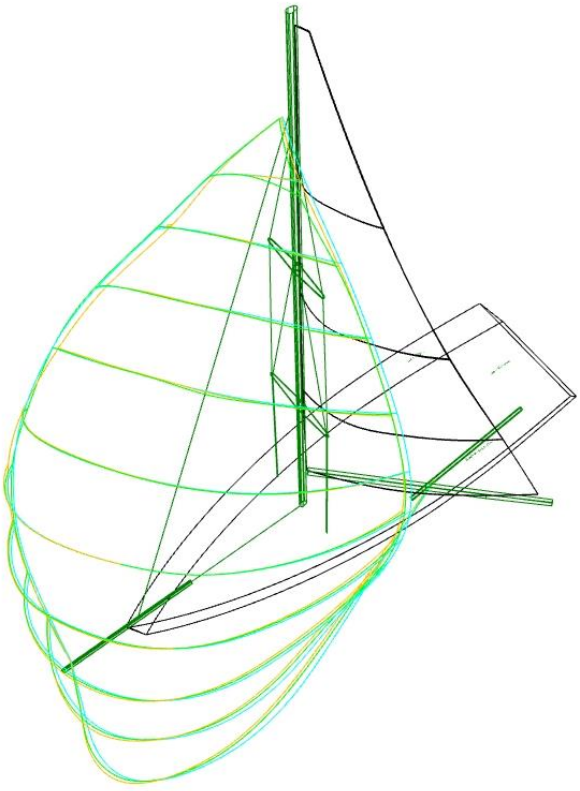

Figure 16: Sail set “A” at an AWA of 105°, three consecutive sets of photos

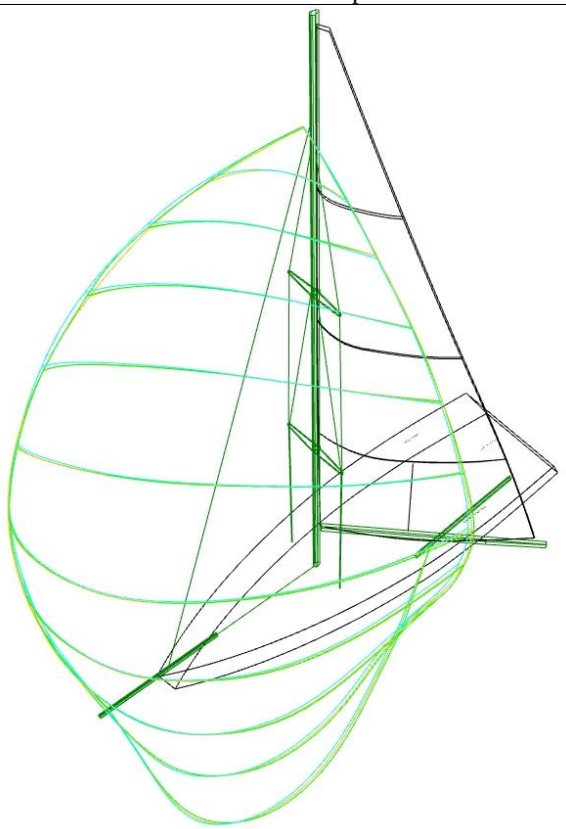

Figure 17: Sail set “B” at an AWA of 90°, three consecutive sets of photos

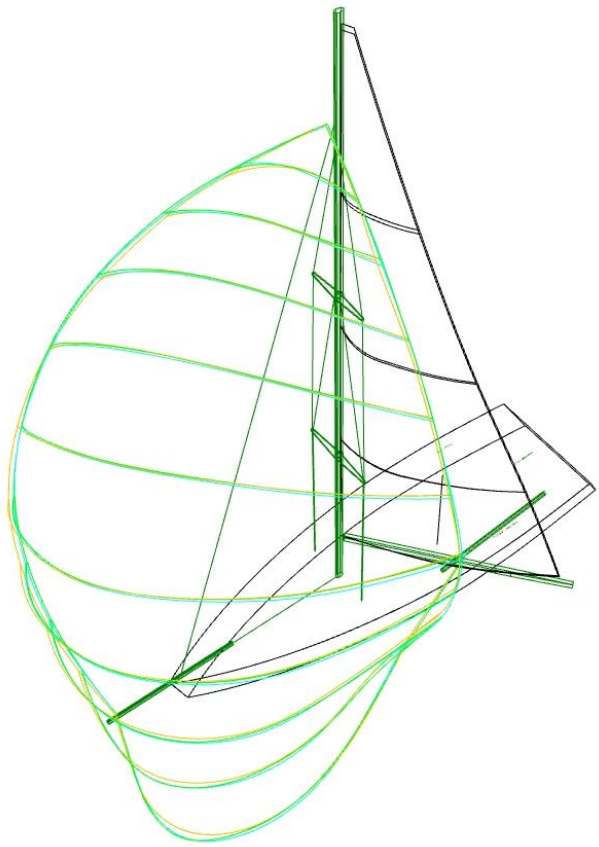

Figure 18: Sail set “B” at an AWA of 105°, three consecutive sets of photos

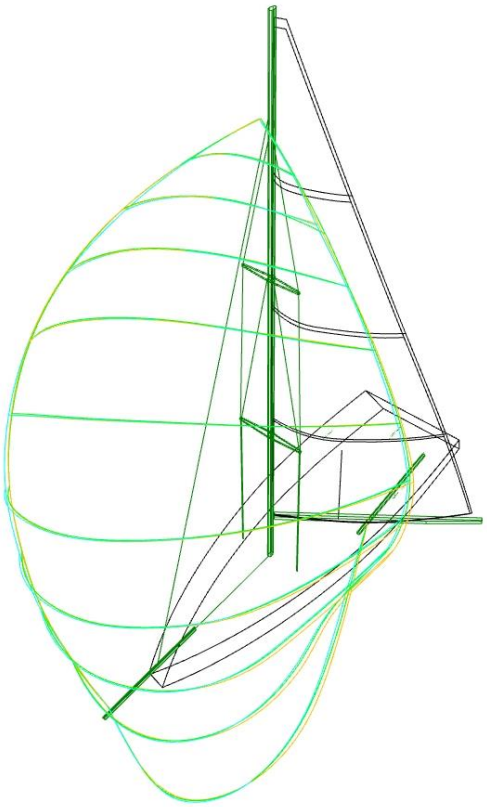

Figure 19: Sail set “B” at an AWA of 120°, three consecutive sets of photos

DYNAMIC STABILITY OF FOILBORNE HYDROFOIL/SWATH WITH ANHEDRAL FOIL CONFIGURATION

(DOI No: 10.3940/rina.ijsct.2017.b2.202)

S Williams, Massachusetts Institute of Technology, USA and **S Brizzolara**, Virginia Tech, USA

SUMMARY

The hybrid hydrofoil/SWATH (Small Waterplane Area Twin Hull) designed and patented by Stefano Brizzolara, is a novel vehicle that is optimized to operate in both a high-speed foilborne mode and a displacement mode. The deployable hydrofoils on the vehicle take on a unique four surface piercing anhedral foil configuration. This foilborne design had previously undergone only preliminary assessment of stability characteristics. A six degree of freedom model of the foilborne vehicle dynamics is introduced as a framework to study vehicle stability and maneuvering. Stability criteria derived from multiple linearized models of the vehicle dynamics are compared to the six degree of freedom results in both the vertical and horizontal planes. Foil configuration design criteria are developed for pitch equilibrium, pitch stability, and directional stability.

NOMENCLATURE

A_{11}, A_{22}	Added mass components
AR	Aspect ratio
A_p	Planform area
A_w	Wetted area
b	Wing span
c	Chord length of foil
C	Courant number
$\hat{C}$	Chord unit vector
C_{di}	Induced drag coefficient
C_l	Lift coefficient
C_p	Pressure drag coefficient
h_w	Wing height over free surface
I	Moment of inertia
K	Roll moment
k	Reduced frequency (Hz)
L	Length of ship
L_a	Length of aft foil
L_f	Length of front foil
M	Pitch moment
M_{munk}	Munk moment
m	Mass of ship
mc	Mean chord
N	Yaw moment
p	Roll rate (deg s^{-1})
q	Pitch rate (deg s^{-1})
r	Yaw rate (deg s^{-1})
Re	Reynolds Number
$\hat{S}$	Span unit vector
SWATH	Small Waterplane Area Twin Hull
T	Submerged foil length
t	Time
t_w	Thickness of wing
U_o	Advance speed
u	Surge rate
v	Sway rate
w	Heave rate
X	Surge force
Y	Sway force
Z	Heave force
α	Angle of attack (deg)
α_{rad}	Angle of attack (rad)
Γ_a	Dihedral angle of aft foil (deg)
Γ_f	Dihedral angle of front foil (deg)
λ	Eigenvalue
υ	Kinematic viscosity of water
ϕ	Roll Euler angle (deg)
ψ	Yaw Euler angle (deg)
ρ	Density
θ	Pitch Euler angle (deg)
ω	Rotation rate (rad s^{-1})
ω_c	Oscillation frequency (rad s^{-1})

1. INTRODUCTION

The hybrid hydrofoil/SWATH vehicle, patented by Dr. Stefano Brizzolara, is one novel design with the potential to push the top speeds of hydrofoil technology (Brizzolara, 2014). The vehicle, shown in Figure 1, has two operating modes. At low speeds, the vehicle operates in displacement mode, powered by twin-submerged propellers, and benefits from superior seakeeping and powering characteristics of the unconventional SWATH design. In foilborne mode, the SWATH hulls fly above the free surface on four anhedral surface piercing ventilated hydrofoils with sections optimized for super-cavitation. When foilborne, the vehicle is powered by direct thrust from two aircraft jet engines on the wing-shaped superstructure.

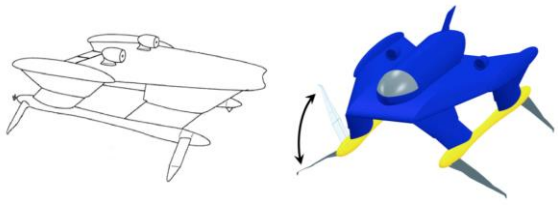

Figure 1: The hybrid hydrofoil/SWATH, unmanned (left) and manned (right) versions

The two modes of the vehicle operate with different lifting principles, and during transition the vehicle operates as a true hybrid supported partially by buoyancy and partially by dynamic lift. The foils are rotationally actuated during the transition between modes. Figure 2 conceptually shows this transition of the vehicle deploying the hydrofoils and taking off from SWATH mode into foilborne mode. The foils do add to the vehicle drag in SWATH mode.

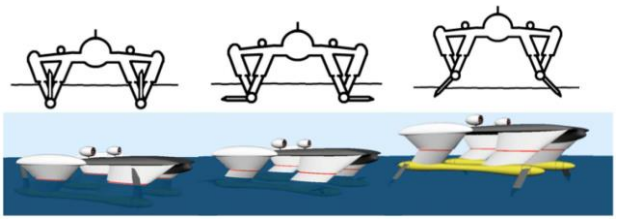

Figure 2: The transition between modes

At speeds above about 50 knots, cavitation becomes inevitable (Acosta, 1973). At these speeds, the hydrofoil section must be optimized to perform with a stable vapor cavity to avoid large unsteady forces due to cavitation. The hybrid hydrofoil/SWATH vehicle employs hydrofoils designed with the SCSB-II super-cavitating section, which has been optimized to maximize performance at speeds up to 120 knots (Bonfiglio and Brizzolara, 2016; Brizzolara, 2015; Vernengo et al., 2016; Bonfiglio and Brizzolara, 2015). Supercavitating foils have lower lift-to-drag ratios than subcavitating foils because the suction side is not generating lift. At their design condition, these foils have been experimentally demonstrated to have a lift-to-drag ratio of about six at a Froude number corresponding to top speed for the full-scale vehicle (Brizzolara et al., 2012).

The four hydrofoils on the vehicle are designed to be surface piercing for variable area stabilization effects in pitch and roll, and to eliminate the need for surface piercing structural members, which are required in fully submerged foil designs. The anhedral or negative dihedral foil angles are a result of the rotationally actuated foil design and the foil packaging issue involved. The foils are rotationally lifted on the outside of the ship when the ship is in SWATH mode, which requires the foils to take a negative dihedral angle when deployed. There is a possibility of a design with foils that could be rotated towards the inside of the hull and therefore take a positive dihedral angle. This would resemble a more conventional "V" shaped surface piercing foil configuration, however, it would introduce potential problems with the foils interfering with each other and the superstructure when rotated. The inward rotating, positive dihedral design would also give the foils significantly less lateral separation, which would tend to reduce the roll stability. The negative dihedral or anhedral foil configuration has the benefits of high maneuverability and enabling quick short radius turns, however, it does tend to make the vehicle less directionally stable (Drela, 2014). An integral part of the foilborne design is that the dihedral angles can be adjusted, not just for transitioning between modes, but also dynamically for trimming and maneuvering the vehicle akin to the use of control surfaces in airplane maneuvering (Williams, 2017).

As the conceptual design of this vehicle progresses, there is a need to understand better the conditions for stable operation and the effects of foil configuration design on stability. In particular, the four surface piercing foil configuration is unexplored in hydrofoil literature. A combination of analytical solutions, numerical simulations, and scale model experiments is ideal for building a comprehensive understanding of the vehicle dynamics. The goal of this study is to explore this range of available resources to develop a better understanding of the vehicle dynamics, and to establish a numerical and analytical framework in the process that can be used in future continuing studies on this vehicle and other high-speed marine vehicles.

The design space considered in this study includes a range of different front and aft foil dihedral angles and foil lengths. Figure 3 shows the how these are defined on the front port foil. The dihedral angle (Γ_f for the front foils) is defined below the horizontal, and foil length (L_f for the front foils) is defined from the tip to center of rotation. The trends in the effects of foil length and dihedrals on stability have been studied in the vertical and horizontal planes using a vehicle dynamics model. The results that these studies show serve as important guidelines for foil configuration design process.

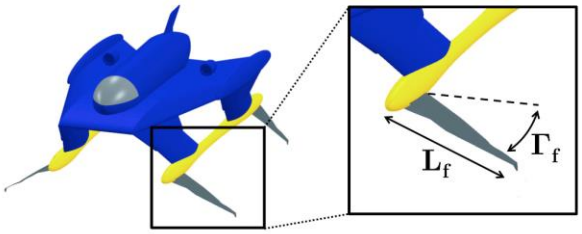

Figure 3: Foil length and dihedral angle definitions

2. VEHICLE DYNAMICS MODEL

2.1 MODEL OVERVIEW

To quantify the effects of vehicle design on stability, a six degree of freedom numerical model of the hybrid hydrofoil/SWATH vehicle in foilborne mode was developed. The model is written in MATLAB, and its computing process is diagrammed in a schematic in Figure 4. The model inputs are kinematic and outputs are the resulting dynamics. The dynamics are calculated by modelling the hydrodynamic, aerodynamic, and engine thrust forces and resulting moments acting on the vehicle at a given state of position, orientation, and motion with six degrees of freedom. The forces are modelled based on a combination of experimental data and theoretical results.

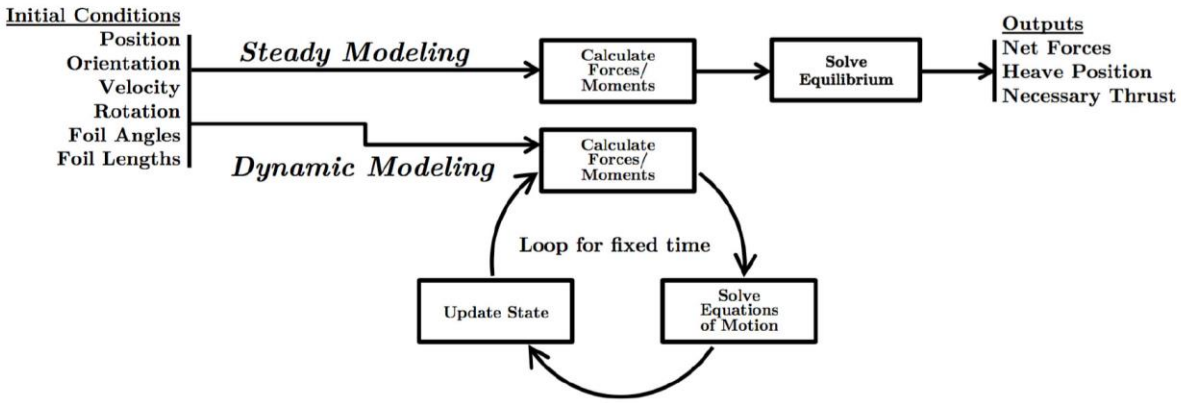

Figure 4: Model block diagram

The model can run in a quasi-steady mode or a fully dynamic mode. In quasi-steady mode, the model can solve for net forces or it can also solve for the heave position and engine thrust necessary to achieve equilibrium. In dynamic mode, it solves for a motion in the time domain resulting from an initial condition. The quasi-steady mode is useful for solving for equilibrium positions and modelling steady manoeuvres, and the dynamic mode is useful for computing vehicle dynamics coefficients, modelling motion response to perturbations, and modelling unsteady manoeuvres. This serves as a powerful numerical toolkit for studying stability and manoeuvring.

The model is generalized to six degrees of freedom in order to be flexible and useful for a range of dynamic cases. The model is also generalized to allow some of the design features to be easily adjustable and input for systematic design studies. Importantly, the foil lengths and dihedrals can be specified as an input. These are the main features that turn out to play a critical role in the interaction of foil configuration design and stability, and they are used as inputs in the parametric design studies.

2.2 VEHICLE SPECIFICATIONS

To run numerical simulations of the vehicle dynamics, a consistent set of physical characteristics of the vehicle must be adopted. For the purposes of the analysis in this study, these characteristics are used from a configuration of this vehicle previously designed for the rapid transport of crewmembers (Georgiadis, 2014). Table 1 provides a full set of these characteristics. The foil lengths and dihedral angles listed in the table are from this previous design, and will serve as a baseline foil configuration.

2.3 COORDINATE SYSTEMS

In order to describe the kinematics and subsequently the physics of the ship in foilborne mode, two different coordinate systems are employed in the numerical models: an earth fixed coordinate system and a body fixed coordinate system with the origin at the ship's centre of gravity. For dynamic modelling, the origins are coincident at time zero.

Table 1: Vehicle Characteristics

Specification	**Value**
Length overall	30 m
Displacement	254,000 kg
Foiling top speed (U_o)	80 knots
Front foil length (L_f)	8.85 m
Aft foil length (L_a)	8.00 m
Front foil dihedral (Γ_f)	40°
Aft foil dihedral (Γ_a)	40°
I_{xx}	1.90×10^7 kgm^2
I_{yy}	4.23×10^7 kgm^2
I_{zz}	5.50×10^7 kgm^2
I_{xz}	-3.09×10^5 kgm^2

The rotational orientation of the body frame relative to the earth frame is defined with *x-y-z* convention Euler angles. In this convention, the coordinate transformation matrix is defined by a roll angle about the body x-axis (ϕ), pitch angle about the body y-axis (θ), and yaw angle about the body z-axis (ψ), in that order. These rotations and the coordinate systems are visualized in Figure 5, where the body frame coordinates shown as green, and the earth frame coordinates shown as black.

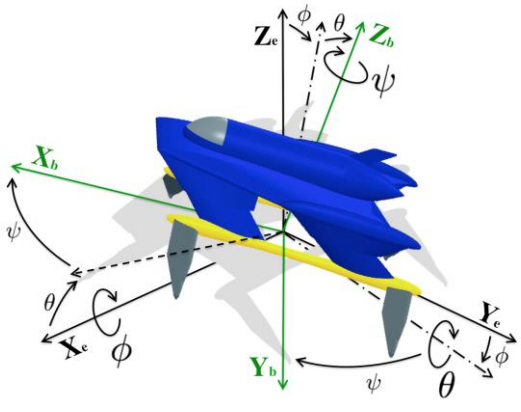

Figure 5: Euler angle rotation definitions

2.4 GEOMETRY OF SUBMERGENCE AND HEAVE

To determine the relationship between the distance of the ship's centre of gravity to the free surface and the submergence lengths of the foils, the model approximates the foils as lines representing the foil span. The free surface is modelled as a plane, under the assumption of a calm sea state, and the model then employs the parametric form of the line-plane intersection within the body frame coordinate system to solve for the foil submergence lengths (O'Rourke, 1998). Given a vehicle orientation in terms of Euler angles, the foil submergence lengths can be calculated using the origin to free surface distance and vice versa. A conceptual representation of the foil submergence modelling of the vehicle is shown in Figure 6 including an example of the set of points necessary to define the problem. For submergence modelling, 3 points define the free surface, 2 points and an intersection with the free surface define each foil, and the vehicle is defined by the origin location and Euler angles.

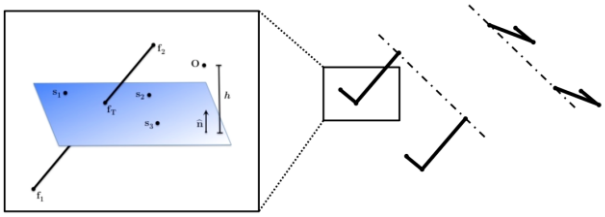

Figure 6: Vehicle and foil submergence model

2.5 MODELING FORCES AND MOMENTS

The forces and moments developed on the vehicle can be described using the coordinate system and Euler angle framework, the positions of the hydrofoils and superstructure, and the kinematics of the inflows. Both the hydrodynamic forces and moments due to the hydrofoils and the aerodynamic forces and moments due to the wing-shaped superstructure are modelled. The substantial difference between the density of water and air results in the hydrofoil forces dominating the vehicle dynamics in foilborne mode. However, the aerodynamic forces still have a non-negligible effect.

The hydrodynamic force on each hydrofoil is calculated based on an interpolation of experimental data collected in scale model free surface cavitation tests (Brizzolara et al., 2012). Figure 7 shows the experimental setup of this cavitation tunnel study of an SCSB-II section surface piercing hydrofoil at a dihedral angle. The flow in the image is from right to left, and the ventilated cavity covers the back of the hydrofoil and only the winglet is visible. The experimentally collected force coefficients are fit to third order polynomial functions of the length of submergence (T) and angle of attack of the foil (α):

$$C_l = f(T, \alpha)$$

This polynomial function is used for interpolating coefficient values within the experimental range of T and α. The 3D foil geometry used in the test is a 1:10 scale model of the full-scale design. The test scale model had a design draft of 250 mm and a root chord at design submergence of 205 mm. The test data covers a range of submergences from 175 mm to 350 mm and a range of angles of attack from -3 to 8. With the tapered planform, the design aspect ratio is approximately 2.5.

In order to apply this interpolated data, the submergence and angle of attack of each foil must be calculated given the length and dihedral angles of the foils, and the orientation and total submergence of the vehicle. The foil span and line-plane intersection routine is used to calculate submergence, and to calculate angle of attack a unit vector is used to represent the chord.

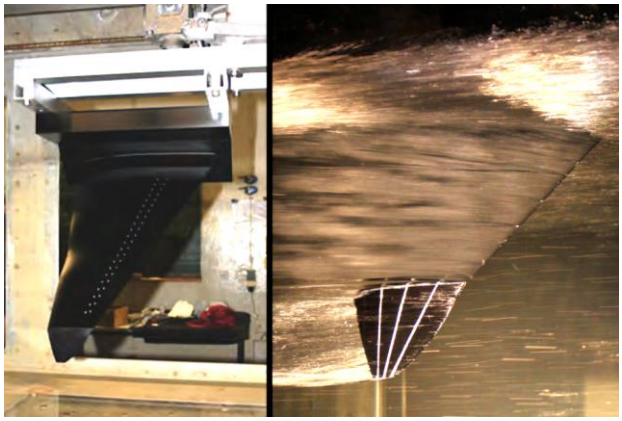

Figure 7: Cavitation tunnel setup (left) and experiment underway with surface piercing, super-cavitating hydrofoil working in its design condition (right)

The inflow that the foils are subjected to is the negative of the vehicle velocity. Unit vectors are used to represent each foil's span and chord, denoted as $\hat{S}$ and $\hat{C}$ respectively. The dot product between the span vector and the inflow velocity vector gives the magnitude of the spanwise component of the flow, which is neglected and subtracted from the flow to determine the effective inflow:

$$\vec{V}_{eff} = \vec{V} - (\vec{V} \cdot \hat{S})\hat{S}$$

Figure 8 demonstrates how the inflow vector is decomposed into spanwise and chordwise components. The angles and relative magnitudes of the flow components in this figure are exaggerated for visualization purposes.

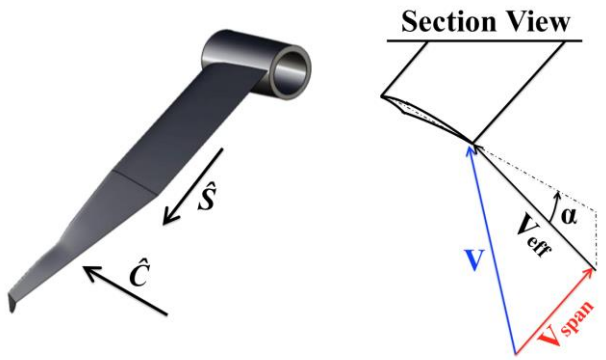

Figure 8: Foil inflow decomposition

The angle of attack in the cross section planes is then determined for each foil using a dot product between the effective inflow and chord:

$$\alpha = \cos^{-1}\left(\frac{\vec{V}_{eff}\cdot\hat{C}}{\left|\vec{V}_{eff}\right|\left|\hat{C}\right|}\right)$$

In the case of dynamical modelling of the vehicle, the foil forces must be applied considering the vehicle's state of angular velocity and acceleration. The model is based on the assumption of quasi-steady foil forces in accordance with Faltinsen's recommendation for calm water hydrofoil dynamics (Faltinsen, 2006). Furthermore, unsteady hydrofoil effects can be verified as negligible using Theodorsen's function, which models deviation from quasi-steady force based on reduced frequency, *k*, of the lifting surface motion, defined as:

$$k = \frac{\omega_c c}{2U_o}$$

Where ω_c is the frequency of oscillatory motion and c is the foil chord length. All the simulated motion results from the model can be shown to fall in the reduced frequency range of $k < 0.1$, in which unsteady forces are negligible compared to quasi-steady forces (Theodorsen, 1935). This applies for the calm water assumption, and if the motion in waves were to be modelled, the unsteady effects due to oscillatory wave forces would not be negligible (van Walree, 1999). This calm water analysis is useful for addressing concerns that negative dihedral design can have initial stability with controls fixed. This is a good foundation for stability in waves, and additionally the rotational actuation of the foils may be employed for closed-loop control in waves.

The effect of vehicle angular velocity on the quasi-steady foil inflow is to add an induced velocity component proportional to the rotation. This is computed based on the centre of force of each hydrofoil (r_i):

$$\vec{V}_{induced} = \vec{\omega}\times\vec{r}_i$$

The aerodynamic forces are calculated for the four struts, the nacelle body, the torpedo SWATH hulls, the wing-shaped superstructure, and the tail fin. The wing structure is modelled as a low aspect ratio wing with ground effect due to the proximity of the free surface. The aerodynamic lift coefficient for the wing superstructure far from the free surface ($C_{l\infty}$) is a function of the aspect ratio and angle of attack (Soeding, 1998):

$$C_{l\infty} = 2\pi\alpha_{rad}\frac{(AR+0.7)AR}{(AR+0.7)^2}$$

The aerodynamic ground effect on the wing superstructure due to the presence of the free surface is also considered. The dominant effect is to reduce the downwash and induced drag of the wing. This is quantified as a function of span of the wing superstructure (*b*) and height of the quarter chord of the wing superstructure above the free surface (h_w) (Hoerner and Borst, 1975).

The increase in lift coefficient due to the ground effect is modelled according to Hoerner:

$$C_l = C_{l\infty}\left(\frac{33(h_w/b)^{3/2}+1}{33(h_w/b)^{3/2}}\right)$$

The aerodynamic drag on the wing superstructure is calculated as a combination of pressure drag, frictional drag, and induced drag (Newman, 1977). The coefficient of friction is calculated using an approximation of Schoenherr's function for frictional drag due to a turbulent boundary layer (Hoerner, 1965):

$$C_f = \frac{0.030}{Re^{1/7}}$$

This approximation is valid for Reynolds numbers in the range of $10^7 < Re < 10^9$. Induced drag is also calculated for the wing (Hoerner and Borst, 1975):

$$C_{di} = C_l\frac{\alpha_{rad}}{2}$$

The pressure drag is also calculated based on the max thickness (*t*) and mean chord length (*mc*) and it is assumed to be proportional to C_f (Hoerner, 1965):

$$C_p = 2C_f\left(1+2\left(\frac{t}{mc}\right)+60\left(\frac{t}{mc}\right)^4\right)$$

The total drag is calculated using the planform area (A_p) and wetted area (A_w) of the wing:

$$D = \frac{1}{2}\rho V^2\left(C_p A_p + C_{di}A_p + C_f A_w\right)$$

The effective inflow velocity and angle of attack on the wing structure are calculated by the same routine as used for the hydrofoils. The four struts connecting the torpedo hull to the wing and the tail fin are also modelled as streamlined bodies with lift and drag forces considered in the same routine as the wing superstructure. The two front struts are modelled with the 20° inward canting angle, measured from the body xz-plane, and similarly the aft struts are modelled with the 20° outward canting angle. The strut canting angles are shown on the vehicle in Figure 1 and are designed to minimize the wake effects in hull-borne operating mode, when the struts are partially submerged (Brizzolara & Chryssostomidis, 2013). The tail fin is centered and vertically aligned. It is designed to contribute to the yaw stability of the vehicle particularly for if it were to become airborne.

The vehicle nacelle body is considered as a streamlined body with just a drag force because it rests on top of the wing. The frictional drag and pressure drag are both calculated in the same routine as used for the struts.

The torpedo hulls, shown in Figure 9, are modelled as slender cylindrical-like bodies of revolution at an angle to the inflow. Experimental results show that the pressure lift and drag force components act in the plane formed by the axis of the hull and the inflow vector, and these forces can be represented together as a force normal to the hull axis with a normal force coefficient (Hoerner and Borst, 1975):

$$C_n = 0.7\sin^2\alpha$$

This is valid for α < 40°, where the angle of attack is between the hull axis and inflow, and the vehicle stays well within this range during regular operation.

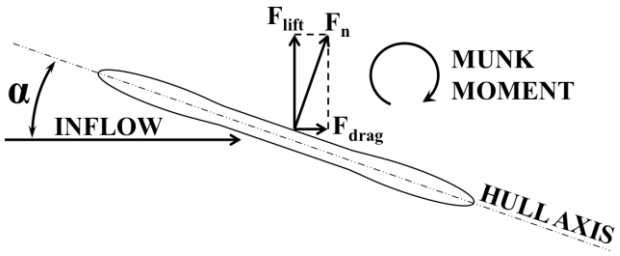

Figure 9: Torpedo hull forces

The Munk moment is also modelled for the torpedo hulls. This moment acts with a vector direction perpendicular to the plane formed by the hull axis and inflow, which can be computed by a cross product. The direction the moment develops is destabilizing in both pitch and yaw. The magnitude can be computed as (Faltinsen, 1993):

$$M_{munk} = \frac{1}{2}V(A_{22} - A_{11})\sin(2\alpha)$$

Where A_{22} and A_{11} are the added mass of the hull in the transverse and axial directions. Using strip theory, A_{22} can be modelled as the sum of the added masses of the circular cross sections, and due to the slender shape of the hull it can be assumed that $A_{22} >> A_{11}$, and A_{11} can be neglected (Newman, 1977).

The final force in the model is the aerodynamic engine thrust. The thrust is assumed to act equally from both engines that sit symmetrically on the wing superstructure 6.7 m above the centre of gravity.

In addition to the forces acting on the vehicle, the moments they induce must also be modelled. To calculate the moments, the centre of each force is determined. The notation of *K*, *M*, and *N* is used for the net moments about the body *x*, *y*, *z* axes respectively, and are calculated by a summation of the cross products of centre of force positions and external forces:

$$Net\ Moment = \begin{pmatrix} K \\ M \\ N \end{pmatrix} = \sum_i \left(\vec{r}_i \times \vec{F}_i\right)$$

2.6 SOLVING THE EQUATIONS OF MOTION

The forces and moments calculated in the model are implemented in the equations of motion in order to solve for the outputs. For quasi-steady analysis, the magnitudes of the thrust and vehicle submergence necessary to achieve equilibrium are treated as unknown variables and solved for with the two force balance equations. This quasi-steady result may include a net moment on the vehicle or a net side force in the y-direction. A true equilibrium solution can be solved for with moments and side force absent by iteratively testing quasi-steady solutions while monitoring the net moment output. An example of this method is the solution to pitch equilibrium demonstrated in Section 3.1.

When modelling dynamic solutions, the six equations of motion derived from conservation of linear and angular momentum are solved numerically using the fourth order Runge-Kutta method (Abkowitz, 1969; Ferziger and Peric, 1999). The convergence of vehicle dynamics solutions using this method has been systematically studied to ensure sufficient convergence and time step independence of the results. Figure 10 demonstrates an example of the rapid convergence of the resulting motion as the time step is refined. The time step is non-dimensionalized using the characteristic length and speed of the vessel and is presented in the form of the Courant number:

$$C = \frac{U_o \Delta t}{L}$$

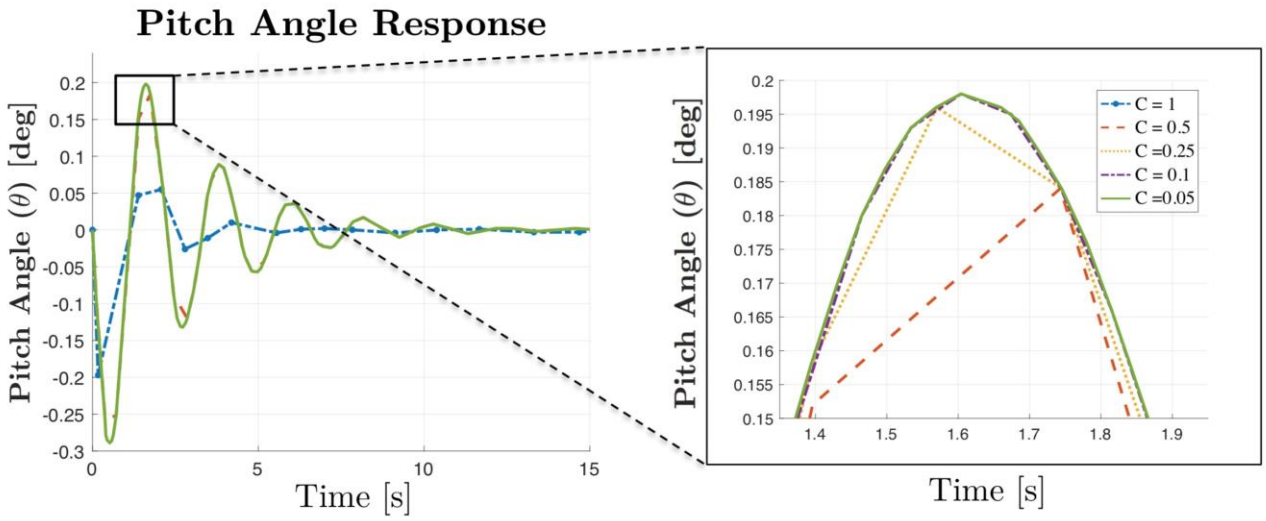

Figure 10: Time step refinement

This representation of the time step corresponds to the number of vehicle lengths travelled during a time step. For example C = 0.02 corresponds to a time step in which the vehicle travels 2% of its length. All of the results of the model presented in the following sections have been verified to be sufficiently refined to below 1% error from the solution with double the step size, which corresponds to C of 0.05 in most cases.

3. VERTICAL PLANE STABILITY

3.1 PITCH EQUILIBRIUM

The first step in analysing stability is to determine the equilibrium point about which the dynamics occur. In the case of vertical plane motion, the equilibrium point is the pitch rotation and heave position at which there is no net heave force, surge force, or pitching moment and the vehicle is at zero trim. Quasi-steady runs of the model can be used to design foil sizes and configurations that satisfy this equilibrium.

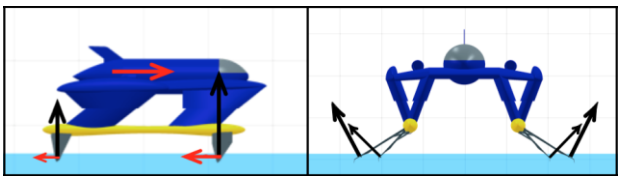

Figure 11: Views of foil forces

The nature of finding pitch equilibrium is affected by the force couple of the engine thrust and foil drag. The centre of thrust above the foil drag creates a strong positive pitching moment. To balance this couple, the fore and aft foils must be used to create a negative pitching moment by generating a larger lift component along the body z-axis with the front foils relative to the aft foils. They are partially helped by the centre of lift of the wing shaped superstructure.

Figure 11 demonstrates this pitching moment balance with the decomposition of force components in the xz-plane. It also demonstrates two main effects of foil length and dihedral on the fore and aft distribution of vertical force from the foils: the first effect is the relative foil submergence length, and the second effect is direction of foil lift. When the foils become more horizontal due to a decreased dihedral angle, more lift force is directed along body z-axis and this gives a higher contribution to the pitching moment.

The design space solved for by the model is mapped in Figure 12. Each graph corresponds to a given aft foil length, and each curve a different aft dihedral. These curves demonstrate the result of how foil lengths must be designed for pitch equilibrium at the specified dihedral angles at top speed. The negative slopes in the results show that when changing the dihedral angle the submergence effects dominate, because increasing the dihedral angle creates a bow-up pitching moment. As the front foils get further from the horizontal they become relatively more submerged and therefore would have to be designed at shorter lengths to maintain pitch equilibrium. Below the curve are a few foil configurations that demonstrate the difference in designs that corresponds to different points on the curves.

These different foil configurations have different stability characteristics that are explored in the following sections. The foils designed with a fixed length, so any single design corresponds to just one point on one of the curves. The focus of this analysis is on stability, but it is also notable that increasing the foil length ratio increases the vehicle efficiency because the aspect ratio of the main lifting surface increases. A ratio of L_f/L_a of about 1.3 is about 10% more efficient (higher vehicle lift-to-drag ratio) than L_f/L_a of 1.

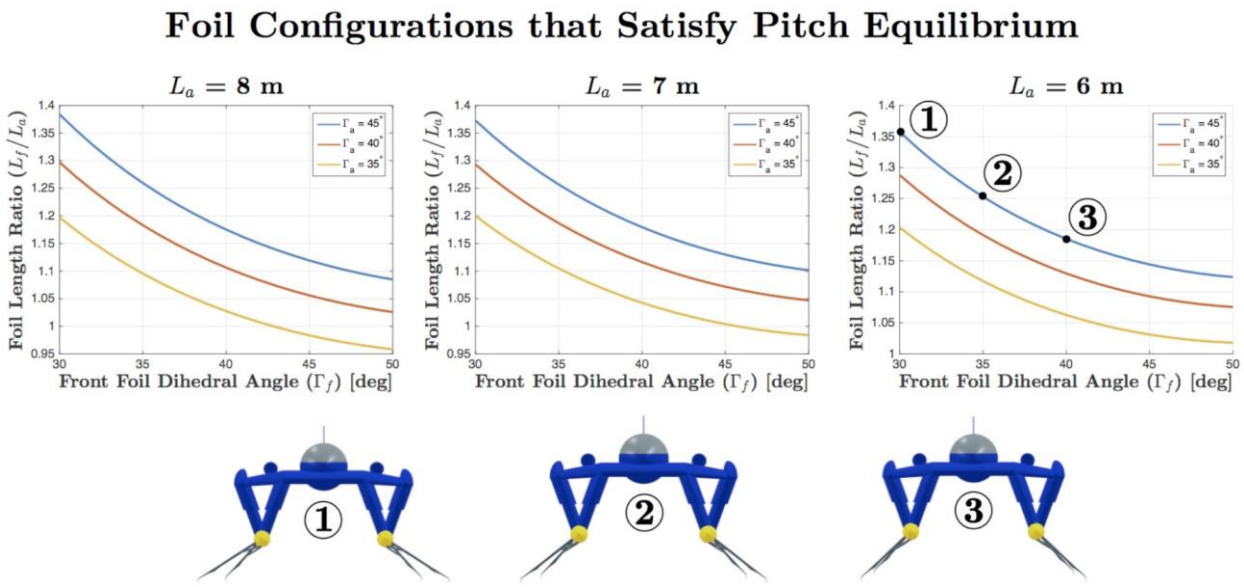

Figure 12: Pitch equilibrium design curves

3.2 LINEARIZED STABILITY CRITERIA IN HEAVE AND PITCH

Comparing six degree of freedom vehicle simulations with simplified analytical solutions can add insight to the stability analysis. Therefore, multiple linearized analytical models of the stability are derived and presented for comparison. These analytical solutions are limited by the small displacements assumption, and by reduced number of degrees of freedom, but if verified by the complete motion simulation, they can provide direct and faster feedback about the effects of foil configuration on stability.

The first linearized model in the vertical plane here presented is limited to just heave and pitch degrees of freedom and surge is neglected. The derivation of the linearized equations of motion in the vertical plane is accomplished by beginning with the nonlinear equations of motion and eliminating all motions other than heave and pitch and dropping higher order terms. The external forces are derived with a Taylor series expansion about the equilibrium, and only the linear terms are considered. These linear terms have coefficients of partial derivatives that are represented by subscript notation (Lewis, 1989). For example, the hydrodynamic coefficient $M_\theta = \partial M/\partial\theta$.

The hydrodynamic coefficients can be determined experimentally, but in the case of this study, they are solved for using the model. The model is nonlinear, as Figure 13 shows, but linearity holds over small angles. To determine M_θ for example M is plotted vs. θ and the slope is taken about equilibrium. Linearity holds for pitch displacements of about ±2° from equilibrium.

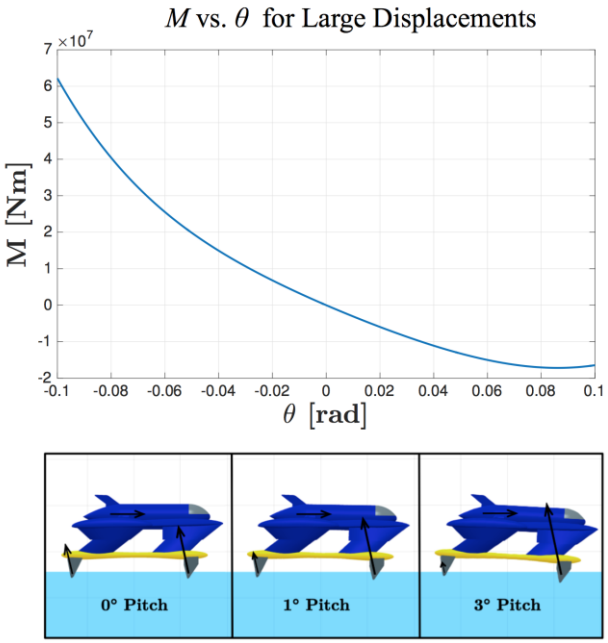

Figure 13: M_θ for baseline foil configuration

The coefficient M_θ specifically is a full speed foilborne equivalent to the longitudinal metacentric height, and is therefore always large and negative (Hamamoto and Kato 1993).

The final simplification is to neglect added mass terms as small under the quasi-steady force assumption (Faltinsen, 1993). This means that terms with coefficients like $M_{\dot{z}}$ and $Z_{\dot{z}}$ are neglected. The heave and pitch equations simplify to:

$$m\dot{w} = Z_\theta\theta + Z_q q + Z_z z + Z_w w$$

$$I_{yy}\dot{q} = M_\theta\theta + M_q q + M_z z + M_w w$$

It is noteworthy that the heave and heave rate here are defined in the earth fixed inertial frame. The equations can be represented in state space as follows:

$$\begin{bmatrix} \dot{z} \\ \dot{\theta} \\ \dot{w} \\ \dot{q} \end{bmatrix} = \begin{bmatrix} 0 & 0 & 1 & 0 \\ 0 & 0 & 0 & 1 \\ \frac{Z_z}{m} & \frac{Z_\theta}{m} & \frac{Z_w}{m} & \frac{Z_q}{m} \\ \frac{M_z}{I_{yy}} & \frac{M_\theta}{I_{yy}} & \frac{M_w}{I_{yy}} & \frac{M_q}{I_{yy}} \end{bmatrix} \begin{bmatrix} z \\ \theta \\ w \\ q \end{bmatrix}$$

The resulting dynamics of this linear system are a combination of exponentials that grow or decay at rates governed by the eigenvalues of the 4×4 matrix of coefficients. Therefore, a necessary and sufficient condition for asymptotic stability is that all the eigenvalues be negative ($\lambda_i < 0$) so any small disturbance in the state exponentially decays back to equilibrium. The analytical solution to the eigenvalue problem gives the specific criteria for stability. These criteria can be based on the derived eigenvalues or equivalently the Routh-Hurwitz stability criteria for the coefficients of the characteristic equation of the eigenvalue problem (Triantafyllou and Hover, 2003).

The result of Routh-Hurwitz analysis of this linear system is a Routh-Hurwitz table of the form:

1	a_2	a_4
a_1	a_3	
b_1	b_2	
c_1		
d_1		

The requirement for stability is that six of these unique indices be positive: a_1, a_2, a_3, a_4, b_1, $c_1 > 0$. In terms of the hydrodynamic coefficients, these indices are:

$$a_1 = -\frac{Z_w}{m} - \frac{M_q}{I_{yy}}$$

$$a_2 = -\frac{Z_z}{m} - \frac{M_\theta}{I_{yy}} - \frac{Z_q M_w}{mI_{yy}} + \frac{Z_w M_q}{mI_{yy}}$$

$$a_3 = -\frac{Z_q M_z}{mI_{yy}} + \frac{Z_w M_\theta}{mI_{yy}} - \frac{Z_\theta M_w}{mI_{yy}} + \frac{Z_z M_q}{mI_{yy}}$$

$$a_4 = -\frac{Z_\theta M_z}{mI_{yy}} + \frac{Z_z M_\theta}{mI_{yy}}$$

$$b_1 = a_2 - \frac{a_3}{a_1}$$

$$c_1 = a_3 - \frac{a_1 a_4}{b_1}$$

The hydrodynamic coefficients can be used to plot how the stability indices vary with different foil configuration designs. This can give a big picture look at stability over a range of designs before running any dynamic simulations. All of the foil configurations tested for stability must first satisfy pitch equilibrium in accordance with Figure 12. The results of this analysis for a few design curves are depicted in Figure 14. The two indices a_1 and a_4 are always large and positive, so they are not plotted. The remaining four indices, a_2, a_3, b_1, and c_1, could potentially become negative and lead to instability.

Figure 14 shows that all of these indices turn out to remain positive over the range of possible designs corresponding to an aft foil length of L_a = 8 m, and aft dihedral of Γ_a = 40°. This trend of stability extends to a range of other aft foil lengths and dihedrals shown in the second plot in Figure 14. The c_1 index is used for other foil designs because it is the index closest to indicating instability. The trend from this plot is that equivalent designs with different foil lengths perform nearly identically, and increasing the aft dihedral angle slightly decreases pitch stability. The most important conclusion is that all designs have very consistently positive indices. This indicates that all designs are stable in the vertical plane according to a linearized model that considers heave and pitch degrees of freedom.

3.3 LINEARIZED CRITERIA IN HEAVE, PITCH, AND SURGE

Coupling heave and pitch for linearized stability analysis in the vertical plane is a good starting approximation, however, surge must also be considered for stability analysis of high-speed marine vehicles (Faltinsen 2006). The equations of motion in the vertical plane are derived following the same method as in the derivation for just heave and pitch motion, but considering perturbation velocities in surge as nonzero. The resulting three coupled linearized equations of motion are:

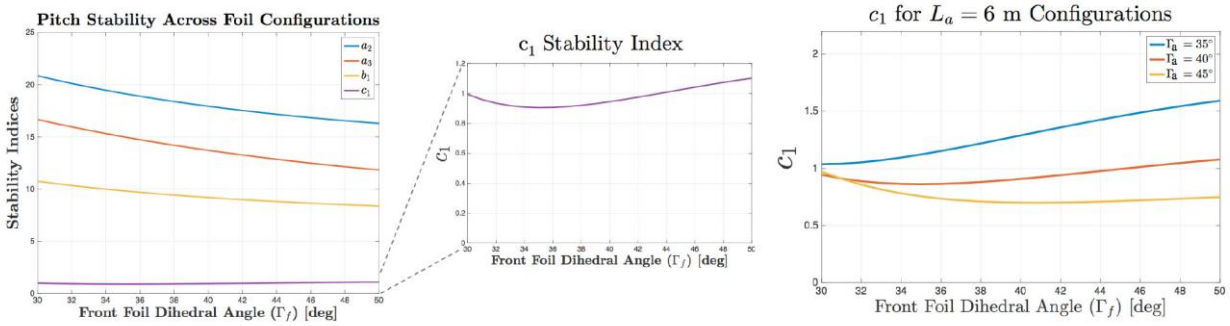

Figure 14: Stability indices across foil designs, the left graph corresponds to $\Gamma_a = 40°$

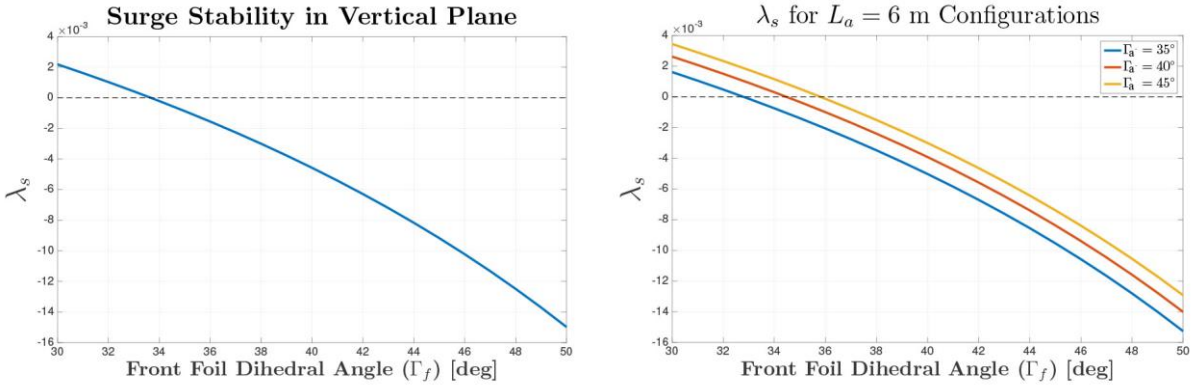

Figure 15: Eigenvalue indication of stability across foil configurations, left graph corresponds to the baseline design

$$m\dot{u} = X_\theta\theta + X_q q + X_z z + X_u u + X_w w$$

$$m\dot{w} = Z_\theta\theta + Z_q q + Z_z z + Z_u u + Z_w w$$

$$I_{yy}\dot{q} = M_\theta\theta + M_q q + M_z z + M_u u + M_w w$$

These equations can be represented in state space as follows:

$$\begin{bmatrix} \dot{z} \\ \dot{\theta} \\ \dot{w} \\ \dot{q} \\ \dot{u} \end{bmatrix} = \begin{bmatrix} 0 & 0 & 1 & 0 & 0 \\ 0 & 0 & 0 & 1 & 0 \\ \frac{Z_z}{m} & \frac{Z_\theta}{m} & \frac{Z_w}{m} & \frac{Z_q}{m} & \frac{Z_u}{m} \\ \frac{M_z}{I_{yy}} & \frac{M_\theta}{I_{yy}} & \frac{M_w}{I_{yy}} & \frac{M_q}{I_{yy}} & \frac{M_u}{I_{yy}} \\ \frac{X_z}{m} & \frac{X_\theta}{m} & \frac{X_w}{m} & \frac{X_q}{m} & \frac{X_u}{m} \end{bmatrix} \begin{bmatrix} z \\ \theta \\ w \\ q \\ u \end{bmatrix}$$

The size of this matrix makes an approach of eigenvalue analysis the clearest method for determining stability. The eigenvalue criterion for stability is that the real part of all eigenvalues must be negative for the dynamic response to be asymptotically stable. The addition of the surge degree of freedom introduces seven new hydrodynamic coefficients.

The 5×5 matrix has one more eignenvalue than the 4×4 matrix. This new eigenvalue is real and corresponds to the surge response. This surge eigenvalue will be denoted as λ_s, and defines the growth or decay of the additional mode introduced by the surge degree of freedom. Figure 15 shows the plot of λ_s over a range of foil configurations, which indicates potential instability of surge response in vertical plane motion.

The other four eigenvalues are negative over the whole design range just as they were without surge. Introducing the surge degree of freedom to the linearized model gives a different assessment of stability. This new eigenvalue suggests that instability occurs when the front dihedrals are about 6° closer to zero than the aft foils. Figure 15 shows that this trend is consistent across a range of designs. Foil length is again shown to have a minor effect. Geometrically similar designs with shorter foils are shown to be slightly less stable. Increasing the aft dihedral away from zero is also shown to decrease stability. As a general rule, all configurations follow the rough criteria that when the front dihedrals are

about 6° closer to zero than the aft foils, the design becomes unstable.

3.4 DYNAMIC RESULTS IN THE VERTICAL PLANE

The linearized models are a tool for looking at vehicle dynamics, but may be limited by their underlying assumptions. The full dynamic six degree of freedom model gives a more thorough description of the vehicle dynamics that can be compared to the linearized models to verify their validity. For motions in the vertical plane, stability can be studied by giving the vehicle an initial condition in equilibrium except for a small perturbation velocity, for instance in pitch. A response motion to this initial condition occurs in heave, pitch, and surge, and may show stable decay or unstable growth of the perturbation.

The first dynamic response case shown from the six degree of freedom model is of the baseline design: Γ_f = Γ_a = 40°, L_a = 8m, L_f = 8.85m. The initial condition given is in dynamic equilibrium except for a pitch rate of q = 0.01 deg/sec. All degrees of freedom are free to respond in the simulation, but due to symmetry only heave, pitch, and surge respond. The response plotted in Figure 16 shows the deviation of these three degrees of freedom from equilibrium. The equilibrium initial forward velocity in this case is 43 m/s. The response shown is stable, as all the motions decay asymptotically towards their equilibrium values. This is in agreement with both of the linearized vertical plane models.

The surge response is plotted in two different time scales to capture fully the nature of the response. The response undergoes a stable oscillation of the same timescale as the heave and pitch response, but also slowly approaches equilibrium well after the oscillations die out. This slow stable response is well predicted by the real eigenvalue of linearized model that includes surge.

The second dynamic response case shown in Figure 16 is of a different design with Γ_f = 32°, Γ_a = 40°, L_f = 9.97m, and L_a = 8m. The same initial condition is applied, and the response is very similar in heave and pitch, however, surge shows a very slow developing instability. The linearized model that includes surge successfully predicts this instability. The eigenvalue criteria specify that when the front dihedral is more than 6° closer to zero than the aft dihedral this instability occurs. This has been verified with disturbances of a small pitch rate, pitch angle, heave position, and heave rate. The verification is of initial stability results from linear models, so only small amplitude perturbations are tested.

This surge instability is of such a slow timescale that in practicality it presents little issue. Any slow feedback control on surge using the engine thrust can easily stabilize the system if a design is chosen that falls into the unstable region. In that case the linearized model with just heave and pitch degrees of freedom is sufficient tool for characterizing the vehicle dynamics in the vertical plane. However, to study the potential instabilities in surge and design the feedback control system, the linearized model that includes the surge degree of freedom is a good tool for predicting these dynamics as verified by the full six degree of freedom simulations.

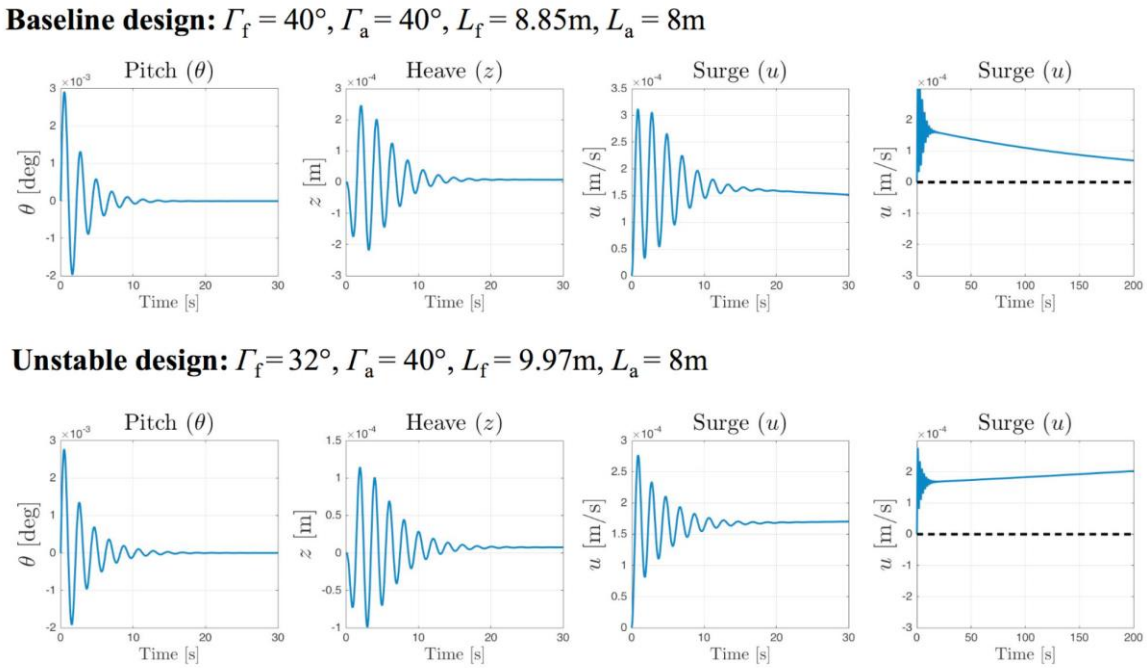

Figure 16: Dynamic responses in the vertical plane

4. HORIZONTAL PLANE STABILITY

4.1 LINEARIZED STABILITY CRITERIA IN SWAY AND YAW

Due to xz-plane symmetry, there are no additional requirements for equilibrium in horizontal plane beyond the equilibrium condition used in the vertical plane. Unlike pitch in the vertical plane, the physical system lacks an absolute reference to heading degree of freedom. Therefore, directional stability in the horizontal plane can be described with varying levels or degrees (Arentzen and Mandel, 1960). The only level of horizontal plane stability possible with controls fixed is returning to a steady heading, not necessarily the original heading prior to a perturbation. This will be the type of directional stability referenced in this analysis.

The linearized equations of motion in sway and yaw are a classic result in ship manoeuvring. The equations are derived in the same way as the vertical plane linearized equations were derived. These simplified equations can be represented in state space:

$$\begin{bmatrix} \dot{v} \\ \dot{r} \end{bmatrix} = \begin{bmatrix} \frac{Y_v}{m} & \frac{Y_r}{m} - U_o \\ \frac{N_v}{I_{zz}} & \frac{N_r}{I_{zz}} \end{bmatrix} \begin{bmatrix} v \\ r \end{bmatrix}$$

The criteria for directional stability based on these equations are another classic result from manoeuvring. In this case, there is only one critical index that is derived from the Routh-Hurwitz analysis, which will be denoted as C_{hp}. This horizontal plane stability index can be used to assess stability, with requirement for stability that it must be positive. The result of the derivation is:

$$C_{hp} = Y_v N_r + N_v \left(m U_o - Y_r \right)$$

The hydrodynamic coefficients are again derived from the model. The term N_v is the critical term for stability and is representative of the yaw linear moment created by a sway motion. This develops as a result of the angle of attack change on the foils in sway and is not a result of submergence effects. The larger the dihedral angle is, the more direct coupling there is between sway and angle of attack. The magnitude of the moment is therefore sensitive to the fore and aft dihedral angles. Having the aft foils at larger dihedrals results in them acting more as fins in the aft, which increases N_v and stability.

The coefficients can be used to plot how the stability index C_{hp} varies with different foil configuration designs. Figure 17 plots C_{hp} for different dihedral designs corresponding to an aft foil length of L_a = 8m and aft dihedral of Γ_a = 40°. The result suggests directional stability is relatively difficult but possible to achieve. The front dihedrals have to be decreased to about 6° less than the aft dihedrals for C_{hp} to become positive and indicate stability. This is directly related to the fin effects in sway due to steeper dihedrals.

The trend across other foil configurations follows as expected. Geometrically similar designs with different foil lengths again show little difference in stability. The slight effect of foil length is that shorter foils lead to slightly more directional stability. The aft foil dihedral effect follows the trend of the fin effect, and steeper aft dihedrals are more directionally stable. Across all configurations, it is a consistent requirement that about 6° steeper dihedral angle away from zero is needed in the aft relative to the front foils for stability.

4.2 LINEARIZED CRITERIA IN SWAY, YAW, AND ROLL

The linearized solution of sway and yaw is the standard tool used for directional stability analysis of displacement ships. A major assumption of that analysis is that the effects of roll motion induced during any horizontal plane disturbance are negligible. Roll effects in manoeuvring of displacement vessels have been shown to be significant in certain cases and particularly at high speeds (Eda, 1908; Logsdon, 1992; Oltmann, 1993; Son and Nomoto, 1981). The assumption of neglecting these effects is applicable to ships with rounded bottoms because the rotational symmetry of the bottom of the hull eliminates roll effects. However, hydrofoil designs like many other high-speed marine vehicles have significant effects induced by roll motion. Therefore, it is necessary to consider the effect of roll on stability and manoeuvring in both foilborne and displacement modes of the hybrid hydrofoil/SWATH.

A linearized model in the horizontal plane that includes roll effects can be compared to the linearized model without roll, and to the six degree of freedom model. The linearized equations of motion in the sway, yaw, and roll degrees of freedom can be represented in state space:

$$\begin{bmatrix} \dot{v} \\ \dot{r} \\ p \\ \dot{p} \end{bmatrix} = \begin{bmatrix} m & 0 & 0 & 0 \\ 0 & I_{zz} & 0 & I_{xz} \\ 0 & I_{xz} & 0 & I_{xx} \\ 0 & 0 & 1 & 0 \end{bmatrix}^{-1} \begin{bmatrix} Y_v & Y_r - mU_o & Y_\phi & Y_p \\ N_v & N_r & N_\phi & N_p \\ K_v & K_r & K_\phi & K_p \\ 0 & 0 & 0 & 1 \end{bmatrix} \begin{bmatrix} v \\ r \\ \phi \\ p \end{bmatrix}$$

With the addition of the roll degree of freedom, eight more hydrodynamic coefficients are needed. Among the new coefficients, K_ϕ is notably related to the equivalent of the transverse metacentric height at full speed. It is defined by submergence effects and is always a large and negative value.

The eigenvalues of the 4×4 matrix are used as stability indices in this case. The results from the eigenvalue analysis show a similar trend to the linearized case of just sway and yaw, but the criteria suggest directional stability is more readily achievable when roll is considered. Figure 18 shows the plot of the eigenvalues

over a range of foil configurations with $\Gamma_a = 40°$ and L_a = 8m. Negative eigenvalues again correspond to asymptotically stable designs. This trend is consistent across a range of designs. Foil length is again shown to have a very minor effect. Geometrically similar designs with shorter foils are shown to be slightly less stable. Increasing the aft dihedral increases stability again due to the dihedral angle effect on sway and angle of attack coupling. As a general rule, all configurations follow the rough criteria that the aft dihedrals must be about 2° steeper than the front dihedrals to ensure stability. This trend still can be described as a fin effect of the aft dihedral foils, but the criteria is much more lenient according to the linearized stability criteria with roll considered. Therefore, one of the linearized models is necessarily inaccurate and the six degree of freedom model must be used for verification.

4.3 DYNAMIC RESULTS IN THE HORIZONTAL PLANE

Unlike in the case of the vertical plane, the different linearized models in the horizontal plane suggest significantly different criteria for designs with controls-fixed stability. The full six degree of freedom simulations of the dynamics can verify which linearized model is more accurate.

The first dynamic response case shown from the six degree of freedom model is of the baseline design: $\Gamma_f = \Gamma_a = 40°$, L_a = 8m, L_f = 8.85m. The initial condition given is equilibrium except for a small yaw rate of r = 0.01 deg/sec. All degrees of freedom are free to respond. The response plotted in Figure 19 shows the deviation of sway, yaw, and roll from equilibrium. The response shown is unstable as predicted by both linearized models, as sway, roll, and heading diverge at increasing rates away from equilibrium in response to the perturbation velocity. This has been verified with disturbances of a small yaw rate, yaw angle, roll rate, and roll angle. The verification is of initial stability results from linear models, so only small amplitude perturbations are tested.

The second dynamic response case shown in Figure 19 is of a slightly different design with $\Gamma_f = 38°$, $\Gamma_a = 40°$, L_f = 9.07m, and L_a = 8m. The same initial condition is applied, and the response is stable as predicted only by the linearized model that includes roll. The linearized model that neglects roll predicts that the response should still be unstable. The six degree of freedom model therefore validates the linearized model that includes roll. If roll is neglected in the linear model, the results are inaccurate.

5. CONCLUSIONS

The studies presented here have produced a number of conclusions about the design of the hybrid hydrofoil/SWATH vehicle with four anhedral surface piercing hydrofoils. The first is that in the range of dihedrals studied, submergence effects due to the surface piercing design dominate when achieving pitch equilibrium. This means that when the foil dihedral angle is increased, more vertical force develops due to submergence and in spite of the decreased efficiency of the direction of lift force.

Another result demonstrated is that stability of foil configurations is readily achievable and largely affected by submergence effects of the surface piercing hydrofoils. Linearization is a very powerful tool when applied properly, and linearized models in both the vertical and horizontal planes are validated by the 6 degree of freedom model. The result is that vertical plane motions are captured well by linearized models in just heave and pitch, except for a slow mode in surge that may become unstable. To capture potential surge instabilities, the surge degree of freedom must be added to the linear model. In the horizontal plane, a linearized model including sway, yaw, and roll captures the dynamics well. As expected for anhedral configurations, the roll degree of freedom is critical to modeling horizontal plane motion, and without it, the motion is not adequately described. A summary of the stability criteria results for the linearized models are in the Table 2.

Table 2: Linearized Stability Criteria

Plane of Motion	**DOF**	**Stability Criteria**	**Verified by 6 DOF**
Vertical	Heave Pitch	All Stable	No
Vertical	Heave Pitch Surge	$\Gamma_f > \Gamma_a - 6°$	Yes
Horizontal	Sway Yaw	$\Gamma_f < \Gamma_a - 6°$	No
Horizontal	Sway Yaw Roll	$\Gamma_f < \Gamma_a - 2°$	Yes

Trends in foil length are shown to have limited effect on the dynamics. Geometrically similar designs with varying foil length are shown to have similar performance in terms of pitch equilibrium, stability, and manoeuvring. Foil length is therefore a design point that is independent from stability concerns, and can be determined based on criteria like ride height, clearance from the free surface, and structural design of the foils.

These results are promising for the continuing study and development of the hybrid hydrofoil/SWATH vehicle, and the numerical model developed should be useful tool in the continuing studies. The results are also applicable to other crafts with surface piercing anhedral foil designs, and furthermore, the methodology presented is applicable to any study on hydrofoil configuration design and its effects on stability.

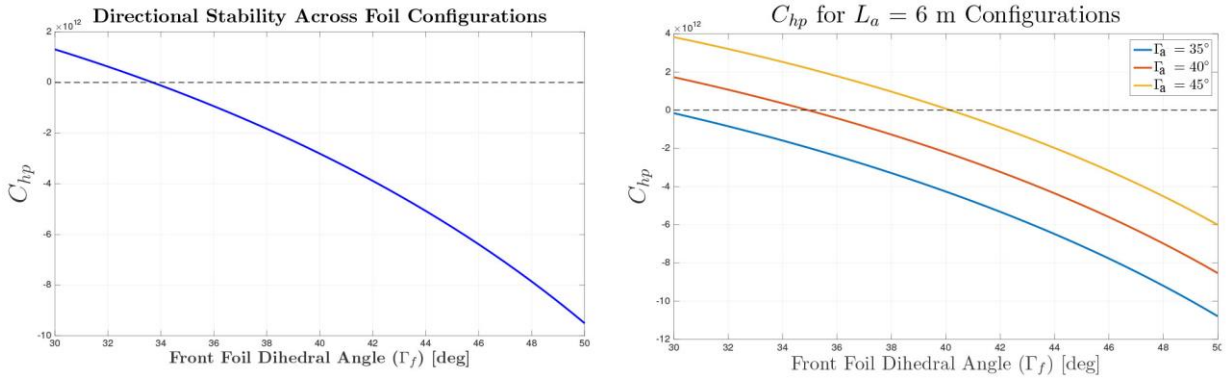

Figure 17: Horizontal plane stability index across foil configurations

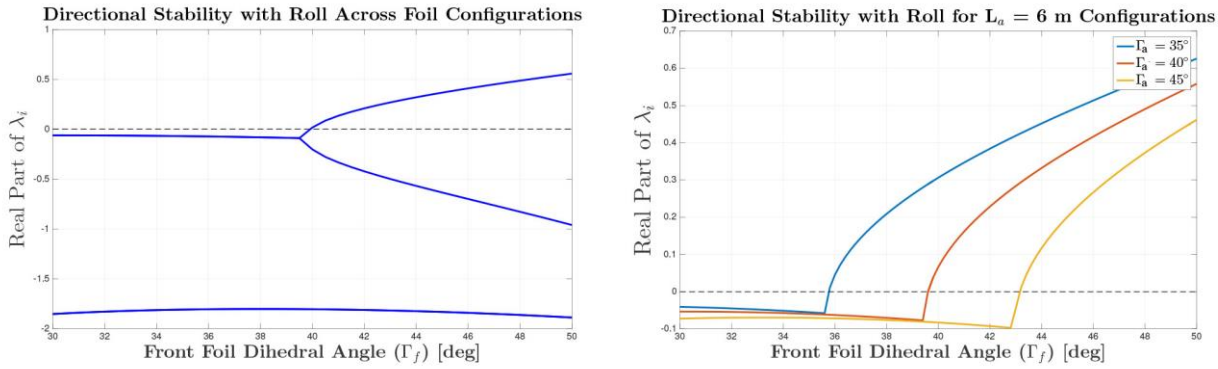

Figure 18: Horizontal plane eigenvalue indication of stability

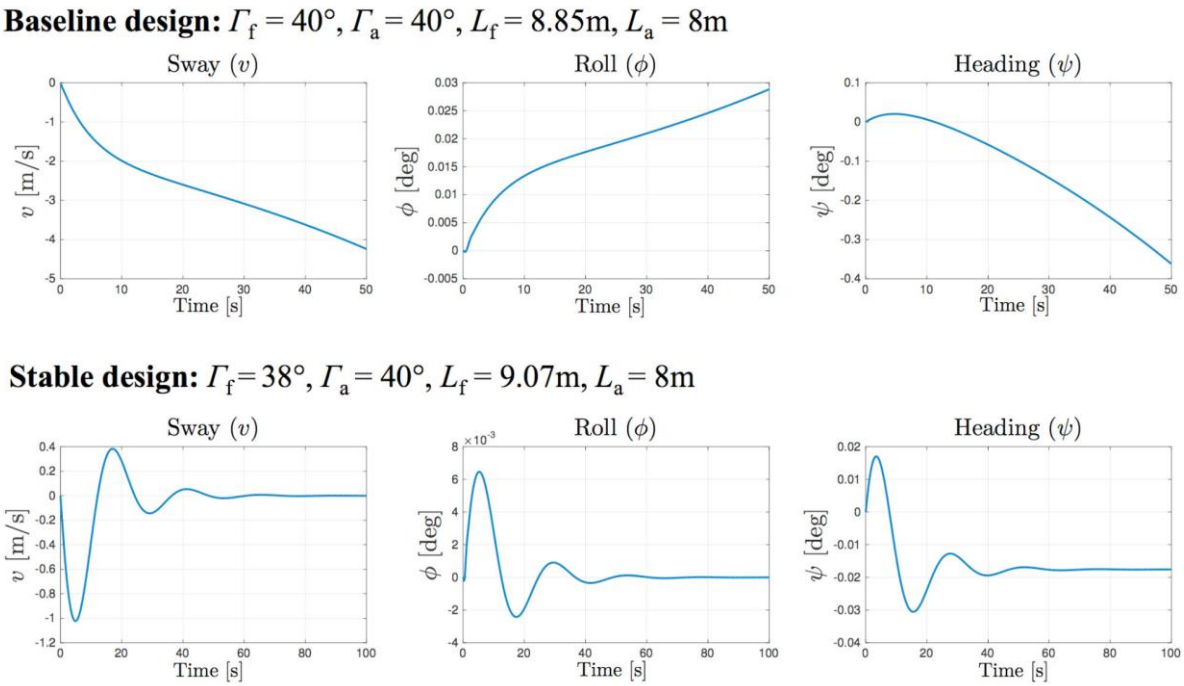

Figure 19: Dynamic responses in the horizontal plane

6. ACKNOWLEDGEMENTS

The authors would like to thank the members of the MIT i-Ship lab for their support of this research.

7. REFERENCES

1. ABKOWITZ, M. (1969). *Stability and Motion Control of Ocean Vehicles*. MIT Press.
2. ACOSTA, A. (1973). *Hydrofoils and hydrofoil craft*. Annual Review of Fluid Mechanics, vol. 322, no. 5, pp. 161–184, 1973.
3. ARENTZEN, E. and MANDEL, P. (1960). *Naval architecture aspects of submarine design*. SNAME Transactions, vol. 68.
4. BONFIGLIO, L. and BRIZZOLARA, S. (2016). *A multiphase RANSE-based computational tool for the analysis of super-cavitating hydrofoils.* Naval Engineers Journal, vol. 128, no. 1, pp. 67–85.
5. BRIZZOLARA, S. (2015) *A new family of dual-mode super-cavitating hydrofoils.* Proceedings of the Workshop on Cavitation and Propeller Performance Fourth International Symposium on Marine Propulsors-smp'15.
6. BRIZZOLARA, S. and BONFIGLIO, L. (2015) *Comparative CFD investigation on the performance of a new family of super-cavitating hydrofoils*. Journal of Physics: Conference Series, vol. 656, no. 1.
7. BRIZZOLARA, S. (2014). *Watercraft device.* US8820260.
8. BRIZZOLARA, S., ECKL, C., and CURA A. (2012) *Forces on a surface-piercing super-cavitating hydrofoil*. tech. rep., UGENOVA-6-2012 for ONR-N62909-11-1-7007 grant.
9. BRIZZOLARA S., CHRYSSOSTOMIDIS C. (2013) *The Second Generation of Unmanned Surface Vehicles: Design Features and Performance Predictions by Numerical Simulations*. ASNE Day 2013, "Engineering America's Maritime Dominance", Feb. 21-22. Arlington, VA.
10. DRELA, M. (2014). *Flight Vehicle Aerodynamics*. MIT Press.
11. EDA, H. (1980). *Rolling and steering performance of high speed ships, simulation studies of yaw–roll–rudder coupled instability*. 13th Symposium on Naval Hydrodynamics, Defense Technical Information Center, Tokyo, pp. 427–439.
12. FALTINSEN, O. (2006). *Hydrodynamics of High-Speed Marine Vehicles.* Cambridge University Press.
13. FALTINSEN, O. (1993). *Sea Loads on Ships and Offshore Structures*. Cambridge Ocean Technology Series, Cambridge University Press.
14. FERZIGER, J. and PERIC, M. (1999). *Computational Methods for Fluid Dynamics*. Springer.
15. GEORGIADIS, V. (2014). *Design and assessment of a super high speed, hybrid hydro-foil/swath crew boat.* Master's thesis, Massachusetts Institute of Technology, Department of Mechanical Engineering, 77 Massachusetts Ave, Cambridge, MA, 02139.
16. HAMAMOTO, M., INOUE, K., and KATO, R. (1993). *Turning motion and directional stability of surface piercing hydrofoil craft*. In Proc. FAST '93 (K. Sugai, H. Miyata, S. Kubo, and H. Yamato, eds.), vol. 1, pp. 807–18, Tokyo: The Society of Naval Architects of Japan.
17. HOERNER, S. and BORST H. (1975). *Fluid-dynamic Lift: Practical Information on Aerodynamic and Hydrodynamic Lift*. Hoerner Fluid Dynamics.
18. HOERNER, S. (1965). *Fluid-dynamic Drag: Practical Information on Aerodynamic Drag and Hydrodynamic Resistance*. Hoerner Fluid Dynamics.
19. LEWIS, E. (1989). *Principles of Naval Architecture*. Society of Naval Architects and Marine Engineers (U.S.).
20. LOGSDON, M. (1992). *Coupled roll and directional stability characteristics of surface ships*. Master's thesis, Monterey, California. Naval Postgraduate School.
21. NEWMAN, J. (1977). *Marine Hydrodynamics*. MIT Press.
22. OLTMANN, P. (1993). *Roll—an often neglected method in ship manoeuvrability*. In Proceedings, MARSIM, vol. 2, pp. 463–471.
23. O'ROURKE, J. (1998). *Computational Geometry in C*. Cambridge University Press.
24. SOEDING, H. (1998). *Limits of potential theory in rudder flow predictions*. 22nd Symposium on Naval Hydrodynamics, Washington D.C., pp. 141–155.
25. SON, K. and NOMOTO, K. (1981). *On the coupled motion of steering and rolling of a high-speed container ship*. Journal of the Society of Naval Architects, Japan, vol. 150, pp. 232–244.
26. THEODORSEN, T. (1935). *General theory of aerodynamic instability and the mechanism of flutter*. NACA Tech. Rep. No 496.
27. TRIANTAFYLLOU, M. and HOVER, F. (2003). *Manoeuvring and control of marine vehicles*.
28. VAN WALREE, F. (1999). *Computational methods for hydrofoil craft in steady and unsteady flow*. PhD thesis, TU Delft, Delft University of Technology.
29. VERNENGO G., BONFIGLIO, L., GAGGERO, S., and BRIZZOLARA, S. (2016). *Physics-based design by optimization of unconventional supercavitating hydrofoils.* Journal of Ship Research, vol. 60, no. 4, pp. 187 – 202.

30. WILLIAMS, S. (2017). *Stability and manoeuvring of hybrid hydrofoil/SWATH in foilborne mode*. Master's thesis, Massachusetts Institute of Technology, Department of Mechanical Engineering, 77 Massachusetts Ave, Cambridge, MA, 02139.

COMPARISON OF MODERN KEEL TYPES FOR SAILING YACHTS

(DOI No: 10.3940/rina.ijsct.2017.b2.203)

K Ljungqvist, SSPA Sweden AB, Sweden, **M Orych**, FLOWTECH International AB, Sweden, **L Larsson** Chalmers University of Technology, Sweden and **C Finnsgård**, SSPA Sweden AB, Sweden

SUMMARY

The performance of three bulb keels is compared with that of a traditional fin keel. Hydrodynamic data from wind tunnel tests are used in a velocity prediction program (VPP) with the keels fitted to a 40' cruising yacht. Two scenarios are investigated: keel retrofitting and new design. In retrofitting, the sail, mast and rig are unchanged, while in new design they are varied to obtain a constant heel angle (Dellenbaugh). Three keel materials are considered: cast iron, lead or a mix thereof. As expected, the bulb keels are superior to the fin keel in all but the lightest winds in the retrofit scenario. The differences between the bulb keels are small, but the keel with a bulb integrated with the fin is slightly slower than the keels with more distinct bulbs, in either L- or T-configuration. These are very close in retrofit, but the T-configuration has a slight advantage in the new design scenario.

NOMENCLATURE

ρ	Density (kg/m^3)
σ	Standard Deviation
A_S	Sail area (m^2)
AR_e	Effective Aspect Ratio (-)
C_D	Drag coefficient (-)
C_{D0}	Viscous drag coefficient (-)
C_{Di}	Induced drag coefficient (-)
C_F	Skin friction coefficient (-)
C_L	Lift coefficient (-)
D	Drag force (N)
E	Base of mainsail (m)
GM	Metacentric height (m)
HA	Heeling arm (m)
I	Height of foretriangle (m)
(1+k)	Form factor
L	Lift force (N)
m	Mass (kg)
n	Number of data points
NM	Nautical Mile (NM)
P	Height of mainsail (m)
S	Wetted Surface (m^2)
T_e	Effective draught (m)
TWS	True wind speed (knots)
U	Velocity (m/s)
VMG	Velocity Made Good (knots)
VPP	Velocity Prediction Program
YD-40	Example Yacht

1. INTRODUCTION

A keel on a sailing yacht has two main objectives, to provide sufficient righting moment and to create a side force that balances the side force from the sails. Traditionally, keels have been fin shaped, but with the increase of sail area more mass is needed to generate sufficient stability. Therefore, the bulb keel has become more common. At an early stage it was mainly racing yachts that used bulbs, but today they are used on most production leisure yachts as well.

To select a bulb type, stability, hydrodynamic performance and practical aspects must be considered. Stability and practical aspects of the bulb are rather straightforward, while hydrodynamic aspects are more complicated. So far, very little has been published on the design of bulb keels for production leisure yachts. Some publications have been presented, i.e. a general discussion on bulb design (Vacanti, 2005), two studies of flow transition of on the bulb (Lurie, 2001) (Böhm & Graf, 2007) and some previous work related to the present study (Ljungqvist et al., 2012), but there is a need for more studies.

The selection of the shape and weight of the bulb for a sailing yacht keel should be carried out at an early phase of the design of the yacht. This is so, since the righting moment from the keel will influence the choice of the rig and sails. Another scenario is the retrofitting of a new keel, where the rig and sails are given. Both scenarios will be addressed below.

The objective of this paper is to investigate the performance of three different types of bulb keels and to compare with a traditional fin keel.

2. METHOD

The performance of the keels was evaluated using wind tunnel tests, described in detail in section 3, and velocity prediction program (VPP) computations, reported in section 4.

3. EXPERIMENTAL SETUP

3.1 DESIGN

In the present project four commonly used keels were tested, three keels with bulb and one conventional fin keel, used as a benchmark. The keels were designed by yacht designer Stefan Qviberg together with

hydrodynamic experts from Chalmers University of Technology. Constant righting moment and draught were two of the design criteria. The lateral area was selected based on the recommendations in Principles of Yacht Design, Larsson *et al.* (2014).

All four keels are presented in Figure 1. K1 is a conventional fin keel that was used as a benchmark. K2 is an integrated L-bulb keel where the bulb gradually merges with the fin and extends behind it. The L-bulb keel (K3) has a distinct transition between the fin and the bulb, which is extended behind the fin also in this case. K4 has a T-bulb extended both in front of and behind the fin. There is a distinct transition between the bulb and the fin. In order to achieve the same righting moment for all keels, the fin keel had to be designed in lead while the other three keels were designed to be made in cast iron.

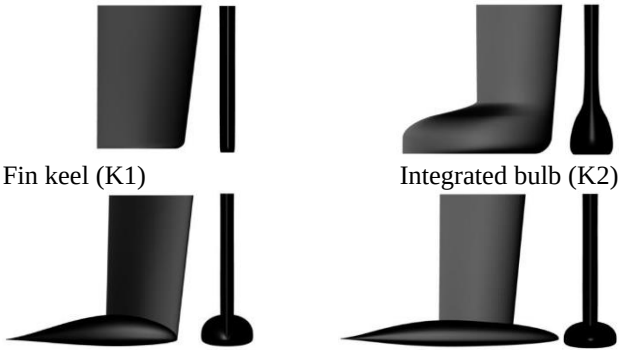

Figure 1: Profile and front view of all four keels.

The fins of all four keels have a NACA 63-015 profile at the top of the blade that gradually changes to a NACA 65-018 at the deepest draft. The bulbs consist of various combinations of NACA 63, 64 and 65 profiles. Further details of the keels are presented in Table 1 and the 3D geometries can be received from the 1st author on request.

3.2 WIND TUNNEL TESTS

3.2 (a) Test Setup

All four keels were tested in the large wind tunnel at the Department of Applied Mechanics at Chalmers University of Technology. The wind tunnel is 1.8m wide and 1.25m high with fillets in the corners tapering off to yield a constant cross section considering the wall boundary layer displacement effect. The length of the test section is 2.7m.

Four keel models were manufactured at a scale of 1:2.5 giving a span of 0.744m. The models were made of NECURON® 651 and CNC milled to the given 3D-geometries. They were also coated and sanded in order to get a smooth surface.

Zigzag tape was fitted along the keels at 25% chord length behind the leading edge, continuing downwards on the bulbs. The purpose of the tape was to force the transition of the flow and thereby trigger a turbulent boundary layer. The thickness of the tape was 0.3mm, which should initiate transition of the flow while maintaining the NACA profile characteristics, (Werner, 2006).

A stethoscope with a needle ending was used to listen to the flow in order to make sure that transition had occurred. As a clear noise could be heard behind the tape but not in front of it, the transition point was located along the tape as desired.

The keels were mounted on a balance below the tunnel floor via two rods that penetrated the floor through very small slots. Different angles of attack were obtained through rotation of the balance.

All tests were carried out at a wind speed of approximately 41 m/s, which resulted in a Reynolds number of 1.04 x 10^6 for keel K2, K3 and K4 and 1.26 x 10^6 for K1 based on the mean chord. The small variations in wind speed and temperature during the measurements would have a negligible effect since the results are presented as force coefficients for drag (C_D) and lift (C_L).

$$C_D = \frac{D}{0.5 * \rho * U^2 * S}\ ,\ C_L = \frac{L}{0.5 * \rho * U^2 * S}$$

where D and L denote drag and lift respectively. ρ is the air density, U the velocity of the wind and S the planform area. In order to make the results for all keels comparable, the planform area of K1 was used for non-dimensionalisation.

3.2 (b) Corrections

The wind tunnel data was corrected as follows:

- Balance alignment (Werner, 2006)
- Keel alignment (Werner, 2006)
- Balance cross coupling (RUAG aerospace defence technology, 2004)
- Solid blockage downwash in the tunnel (Ranzenbach & Zahn, 2005)
- Wake blockage in the tunnel (Maskell, 1963)
- Gap between keel and wind tunnel floor
- Slots for the rods
- Tape drag
- Zero tare

The first 5 listed correction methods are explained in the indicated references and a summary of the correction method used in this project can be found in (Axfors & Tunander, 2011). The final 4 corrections are explained below.

The gap between the keel and the wind tunnel floor was 4mm which is 0.53% of the span of the keel. According to (Barlow *et al.*, 1999) the gap should be below 0.5% of the

span in order to have a negligible effect on the results. However, systematic test were carried out in order to see the effect of the gap, (Axfors & Tunander, 2011), and it was concluded that this effect could be neglected. The reason for the relatively large distance between the keel and the tunnel floor was to prevent the keel from touching the wind tunnel floor at higher speeds.

It was further investigated how the two slots in the wind tunnel floor affected the results, (Axfors & Tunander, 2011). The conclusion was that the effect of the slots could be neglected.

The added drag caused by the zig-zag tape was subtracted from the results. The magnitude of the drag was obtained from (Werner, 2006).

All readings were zeroed before every consecutive run.

3.2 (c) Errors

In the evaluation of the results both bias and precision errors were considered. Bias errors are the calibration errors that are not corrected. This includes errors for:

- Balance
- Pitot tube
- Thermometer

All these errors could be disregarded since they only have a marginal effect on the results. The effect on drag is around 1% and the effect on lift is less than 0.1%. Further details about the bias errors for these tests are presented in (Axfors & Tunander, 2011).

Precision errors refer to the repeatability of the tests and can be estimated by the standard deviation in repeated tests. This was obtained by running several consecutive tests at the same angle with everything dismounted between the tests. The standard deviation could then be calculated as

$$\sigma = \sqrt{\frac{\sum_{i=1}^{n}(y_i - f_i)^2}{n}}$$

where n is the number of data points, y_i is the observed value and f_i the fitted value. The components included in the precision error were:

- Balance precision
- Balance alignment
- Keel alignment
- Angle measurement
- Static pressure deviation
- Temperature deviation
- Effect of varying Reynolds number

The standard deviation is presented in Table 4.

4. PERFORMANCE EVALUATION

The performance of the keels was evaluated using a VPP, the WinDesign developed by the Wolfson Unit at the University of Southampton (Wolfson Unit, 2003). An example yacht, the YD-40 (Larsson & Eliasson, 2007), was used in the analysis, together with the hydrodynamic coefficients obtained in the wind tunnel.

In previous papers on this work the evaluation of the keel performance was made for constant righting moment, (Ljungqvist et al., 2012). This was accomplished by making the fin keel in lead and the bulb keels in cast iron. To fully exploit the benefits of the bulb keels they could be made in lead as well, or alternatively, with the keel blade in cast iron and the bulb in lead. These two possibilities are investigated here, with two different constraints: constant sail area (keel retrofitting) and constant heel angle (new design). Thus in the performance evaluation presented in this paper the combined differences of hydrodynamic and hydrostatic effects of the keels are taken into account. The pure hydrodynamic differences between the keels can be seen in the wind tunnel results but also in the performance evaluation presented in the previous paper (Ljungqvist et al., 2012).

4.1 DESCRIPTION OF THE YD-40

The particulars of the yacht can be found in Principles of Yacht Design, (Larsson & Eliasson, 2007). This data was used in the VPP together with the keel data from the wind tunnel and the geometric CAD definitions. The length overall, LOA of the YD-40 is 12.05m, the maximum beam B_{max} 3.71m and the mass m_{yacht}=4870kg, where the mass of the keel is not included. A two-sail setup including a jib and a main sail was used in the analysis, thus, no downwind sail was included.

4.2 INTRODUCING THE WIND TUNNEL RESULTS

Hydrodynamic coefficients from the wind tunnel tests were introduced in the VPP by the methodology explained below.

- The viscous resistance of the keels was considered by adjusting the wetted surface S_W, introduced in WinDesign. This was done using a form factor, such that

  $$S_W = (1 + k)S_{W\_geo}$$

  Where S_{W_geo} is the geometrical wetted surface for the keel obtained from the 3D geometry and (1+k) is the form factor. This was obtained as the ratio of the viscous drag coefficient C_{D0} measured at zero angle of attack and the skin friction coefficient C_F according to the ITTC -57 formula, (Larsson & Raven, 2010)

$$(1+k) = \frac{C_{D0}}{C_F}$$

- Instead of using the real draught of the keel, the effective draught T_e from the measurements was used in the VPP. By doing so the induced drag of the keel will be correctly computed. The effective draught was calculated according to (Orych et al., 2008) by the formula

$$T_e = \sqrt{\frac{AR_e * S}{2}}$$

where S is the planform area of the keel and AR_e the effective aspect ratio.

$$AR_e = \frac{C_L^2}{\pi * C_{Di}}$$

C_L is the lift coefficient derived from the wind tunnel tests and C_{Di} the induced drag coefficient calculated from

$$C_{Di} = C_D - C_{D0}$$

In this formula, C_D is the total drag coefficient at a given angle of attack and C_{D0} is the drag coefficient at zero angle of attack.

The technique inherently assumes that the increase in viscous drag is proportional to lift squared. This assumption was shown to be appropriate since the results followed a parabolic function when the data was analysed.

4.3 SCENARIO 1: CONSTANT SAIL AREA

In the first VPP computations the sail area was kept constant. The keels were assumed completely made of lead (L), completely of cast iron (CI) and a mix, where the bulb was manufactured in lead while the fin was made of cast iron (L+CI). The properties of the YD-40 including the different keel options are presented in Table 1.

4.4 SCENARIO 2: CONSTANT DELLENBAUGH ANGLE

In the second round of VPP computations the keels were investigated with a variable sail area. By doing so the full potential of the keels could be compared, as the yacht could carry more sails with the keels generating a higher righting moment. As stability criterion the Dellenbaugh angle was used. This is defined in (Larsson et al., 2014) as

$$Dellenbaugh\ angle = 279 * \frac{A_S * HA}{m * \overline{GM}}$$

where A_S is the sail area, HA is the heeling arm, m the mass of the yacht and GM is the metacentric height. In this scenario, the Dellenbaugh angle was set to 14° for all keel variants used in Scenario 1. This corresponds to the value for keel K1 made of lead with the original sail setup. The mast height for the rest of the keel configurations was varied so that the desired Dellenbaugh angle was achieved. Sail dimensions were varied based on the mast height as follows:

$$P_{new} = P_{Base\ case} * \frac{mast\ height_{new}}{mast\ height_{base\ case}}$$

$$E_{new} = E_{Base\ case} * \left(\frac{\left(\frac{mast\ height_{new}}{mast\ height_{base\ case}} - 1 \right)}{2} + 1 \right)$$

$$I_{new} = I_{Base\ case} * \frac{mast\ height_{new}}{mast\ height_{base\ case}}$$

Table 1: Yacht and keel properties for all four keels when manufactured in different materials. L=lead, CI=Cast iron and L+CI=bulb made of lead and fin of cast iron. The sail area for the yacht in all different configurations listed in the table is 71.8 m^2.

	Keel Mass [kg]	**Lateral area [m^2]**	**Root chord [m]**	**Tip chord [m]**	**Keel wetted surf. [m^2]**	**Mass of yacht [kg]**	**VCG, yacht [m]**
K1 CI	1944	2.26	1.33	1.1	4.75	6814	0.19
K1 L	3144	2.26	1.33	1.1	4.75	8014	-0.06
K2 CI	2702	1.84	1.08	0.9	5.25	7572	-0.12
K2 L	4370	1.84	1.08	0.9	5.25	9240	-0.43
K2 L+CI	3836	1.84	1.08	0.9	5.25	8706	-0.38
K3 CI	2687	1.84	1.08	0.9	5.6	7557	-0.12
K3 L	4345	1.84	1.08	0.9	5.6	9215	-0.44
K3 L+CI	3662	1.84	1.08	0.9	5.6	8532	-0.37
K4 CI	2723	1.84	1.08	0.9	6	7593	-0.14
K4 L	4404	1.84	1.08	0.9	6	9274	-0.46
K4 L+CI	3718	1.84	1.08	0.9	6	8588	-0.39

Where P is the height of the mainsail, E the base of the mainsail and I the height of the foretriangle.

As a consequence of the change in sail area the mast and shroud cross-sections had to be adjusted. Thus, the masses of the shortest and tallest rigs where determined and the intermediate values were linearly interpolated between those in order to get the rig weight for each setup. Both stability and displacement changes were considered as a consequence of the changed rig weight.

The properties of the YD-40 for the different keel options, different sail area and different rig size are presented in Table 2.

Table 2: Yacht properties for all four keels manufactured in different materials. L=lead, CI=Cast iron and L+CI=bulb made of lead and fin made in cast iron. The keel properties are the same as presented in Table 1.

	Mass of yacht [kg]	**VCG, yacht [m]**	**Sail area, [m^2]**
K1 CI	6745	0.08	61.9
K1 L	8014	-0.06	71.8
K2 CI	7560	-0.13	70.1
K2 L	9333	-0.3	83.9
K2 L+CI	8774	-0.29	80.7
K3 CI	7546	-0.14	70.3
K3 L	9310	-0.31	84.1
K3 L+CI	8592	-0.28	79.7
K4 CI	7585	-0.15	70.7
K4 L	9374	-0.32	84.7
K4 L+CI	8653	-0.29	80.3

5. RESULTS AND DISCUSSION

In this section, the result from the wind tunnel tests and VPP simulations will be presented and discussed.

5.1 WIND TUNNEL RESULTS AND DISCUSSION

Measured drag and lift coefficients are presented in Table 3 along with the standard deviation based on three repeated tests where the keel was completely dismounted from the tunnel between each test series. To obtain the standard deviation a fourth order polynomial was fitted to the drag data and a linear fit was made to the lift. Note again that all coefficients are based on the wetted area of K1 to enable a direct comparison.

The fitted drag coefficient curves are presented graphically in Figure 2. K1 has the lowest drag due to its much smaller wetted surface. Surprisingly enough, K4 has the lowest drag of the bulb keels, indicating that the extra area due to the long bulb does not cause a drag increase. The form factor is lowest for this keel. K3 exhibits an interesting shape of the drag curve differing from the others, with a smaller drag increase with angle of attack.

Table 3: Measured coefficients (x103) for drag and lift.

	C_D x 10^3			**C_L x 10^3**		
AoA	**0°**	**2°**	**4°**	**0°**	**2°**	**4°**
K1	10.8	12.2	16.5	0	115	228
K2	13	14.4	18.5	0	110	222
K3	12.9	14	17.5	0	108	213
K4	12.1	13.5	17.5	0	110	223

Table 4: Standard deviation (x10^3) of the curve fits

	K1	**K2**	**K3**	**K4**
C_D (AoA) x 10^3	0.14	0.37	0.43	0.32
C_L (AoA) x 10^3	0.39	0.54	0.72	0.61
C_D (C_L^2) x 10^3	0.19	0.47	0.35	0.43

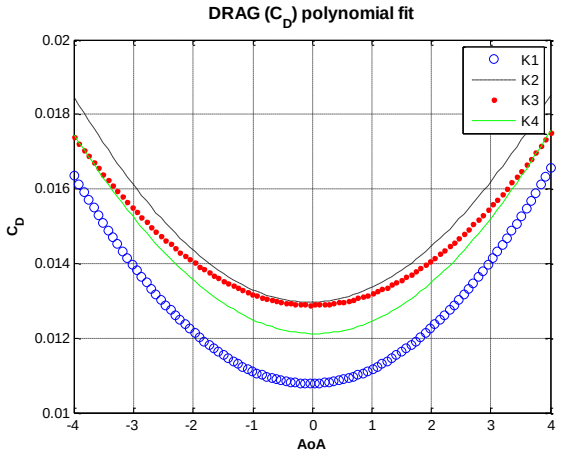

Figure 2: Drag coefficients for all different keels plotted against angle of attack. The data is plotted as fourth order polynomial fits.

This effect is shown also in Figure 3, displaying drag as a function of lift squared. Also in this case a linear fit to the data was made. It is seen that the slope of K3 and K4 is smaller than that of the other two keels. This means the effective aspect ratio is larger for K3 and K4. There is thus an indication that the non-integrated bulbs prevent the overflow better than the others. Due to the effect of the viscous resistance, the drag level for K1 is considerably lower than for the other keels.

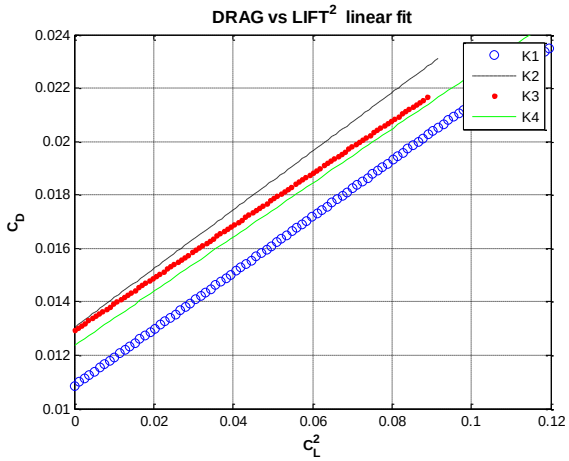

Figure 3: Drag plotted against lift squared. The data is plotted as linear fits.

The standard deviation of the coefficients presented in Table 4 is generally smaller than the differences between the keels, which may thus be considered relevant.

5.2 VPP RESULTS

Results of the VPP simulations will now be presented for the two different scenarios.

5.2(a) Scenario 1: Constant sail area (retrofit)

In Figure 4 the time difference is seconds between the keels is presented for sailing one nautical mile (NM) against the true wind. It is thus a measure of the velocity made good, VMG. The differences are computed relative to K1, made in lead, and are given for four wind velocities: 8, 12, 16 and 20 knots. In each diagram there are three groups of bars, representing cast iron (CI), lead (L) and lead+cast iron (L+CI), respectively.

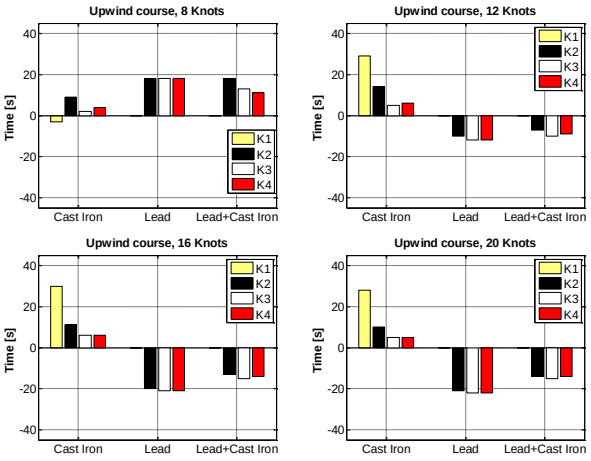

Figure 4: Time difference (s) for a 1 NM upwind course for the different keels at 8 knots, 12 knots, 16 knots and 20 knots true wind speed. All times are compared to the results of K1 L.

At the lowest wind speed stability is not an issue, and the performance is determined by the keel drag, as given in Figure 3, together with the keel weight, which determines the displacement of the yacht. The fin keel is the best since it has both the smallest drag and the smallest weight. Cast iron is slightly better than lead, due to its lower weight. Of the bulb keels, K2 has the largest drag and is the heaviest of the mixed material keels, while it is intermediate in weight for the other materials. Therefore, it does not perform as well as K3 and K4. These are very close. K3 has a slightly higher drag, but is also slightly lighter than K4 and these effects cancel each other to a large extent.

The other three charts of Figure 4 are very similar in trends. Stability is an issue at all wind speeds (12, 16 and 20 knots). Therefore, K1 in cast iron is by far the worst, followed by K1 in lead. K3 and K4 are again very close, with perhaps a slight edge for K3. K2 is worse due to the larger drag.

In Figure 5 the same information as in the previous figure is presented, but for an upwind-downwind course, 1 NM in total length. At the lowest wind speed the figure is almost unchanged. The only important difference is the even larger benefit of the lightest keel, K1 in iron. The very similar appearance of Figures 4 and 5 at 8 knot is due to the fact that the drag difference between the keels is rather independent of the sideforce (see Figure 3), i.e. it does not matter if the hull goes upwind or downwind. It is the viscous resistance, rather than the effective aspect ratio that gives the differences.

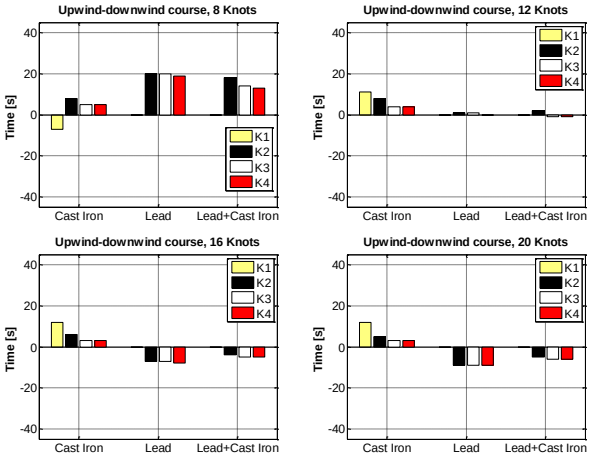

Figure 5: Time difference (s) for a 0.5 + 0.5 NM upwind-downwind course for the different keels at 8 knots, 12 knots, 16 knots and 20 knots true wind speed. All times are compared to the results of K1 L.

For the other three wind speeds in Figure 5 the differences between the reference, K1 L, and the others are smaller than in Figure 4. The reason for this is the smaller fraction of the total resistance that comes from the keel when the speed increases in the downwind course. The wave resistance will then be more dominant.

At 12 knots of wind, all four lead keels are equal, while there is a very small edge for K3 and K4 in mixed materials. There is also a very small advantage of K3 and K4 at the other wind speeds. The reasons are the same as for pure upwind sailing.

5.2(b) Scenario 2: Constant Dellenbaugh angle (new design)

The results from the VPP simulations with constant Dellenbaugh angle, including different sail area and mast dimensions are presented below. Time differences for upwind sailing are shown in Figure 6.

The most striking difference between Figures 6 and 4 is the completely different results at 8 knots. While in Figure 4 the sail area was kept constant for all keels, the area in Figure 6 is adjusted to give the same heel angle for all keels in a moderate breeze (the Dellenbaugh angle). This means that the fin keels, with much lower stability, will call for a much reduced sail area. As seen in Figure 6 this is detrimental to their performance. Particularly the cast iron keel performs very badly at this wind speed.

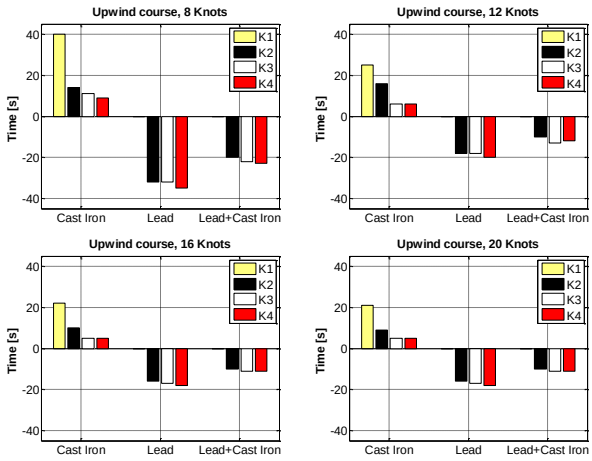

Figure 6: Time difference (s) for a 1 NM upwind course for the different keels at 8 knots, 12 knots, 16 knots and 20 knots true wind speed. All times are compared to the results of K1 L.

Of the bulb keels, K2 performs consistently worse than K3 and K4. This holds for all wind speeds and materials, even if the difference is small in some cases. There is a very small difference in centre of gravity with the different bulb keels, as expected, since they were designed to be equal in this respect (with a uniform density). The worse performance of K2 is primarily attributed to its larger resistance. In terms of weight it is intermediate, except for the mixed material variant, where it is heaviest. There is a slight edge for K4 compared with K3 at most speeds and materials. This is in spite of the fact that is is 40-60 kg heavier. On the other hand, it has lower resitance, and its centre of gravity is one cm lower.

In Figure 7 the results for an upwind-downwind course are presented. Since leeway is much reduced downwind (even if the course is not straight downwind) the resistance of the keels for smaller angles of attack will play a larger role than upwind. In Figure 2 it appears that K2 is then close to K3, while K4 is the best (of the bulb keels). This means that including the downwind leg the relative performance of K2 and K3 will change somewhat compared to upwind only. Such a shift is seen in Figure 7. K2 has now improved relative to K3, and they are now equal, on the average. K4 is now clearly the best keel.

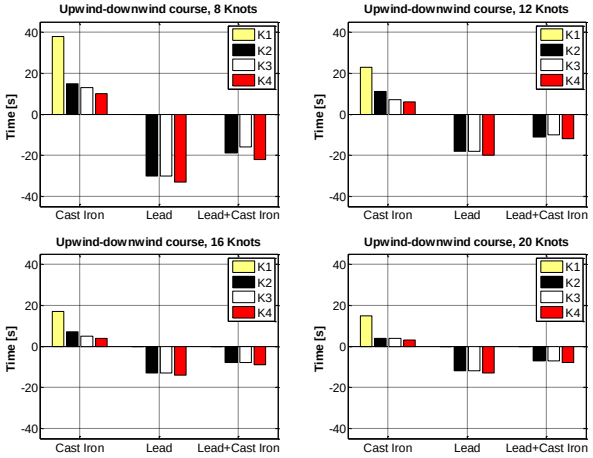

Figure 7: Time difference (s) for a 0.5 + 0.5 NM upwind-downwind course for the different keels at 8 knots, 12 knots, 16 knots and 20 knots true wind speed. All times are compared to the results of K1 L.

6. CONCLUSIONS

In this paper the performance of three different bulb keels has been compared with that of a fin keel. The hydrodynamic qualities of the keels were determined in wind tunnel tests, and the performance was evaluated using a well-known VPP. Two scenarios were considered: retrofitting, where the keel was fitted to a hull with the rig and sails unchanged, and new design, where the rig and sails were adjusted to give the same Dellenbaugh angle for all keels. Three keel materials were used: cast iron, lead and a mix, where the bulb was made in lead and the fin in cast iron. The findings were as follows:

- Due to its smaller wetted surface the fin keel had the smallest drag for all leeway angles tested (up to 4 degrees)
- At low angles of attack the T-keel had the smallest drag of the bulb keels, in spite of its larger wetted surface, while the L- and integrated keels were close in drag. At higher angles the T and L-keels had a very similar drag, while that of the integrated keel was larger.

- The drag increased linearly with lift squared and the slope was larger for the fin and integrated keels than for the other two, indicating that the more distinct transition between fin and bulb of the L- and T-keels prevents overflow and has an endplate effect.
- In the retrofitted scenario the fin keel was superior to the bulb keels at low wind speeds (8 knots). For the best material (cast iron) the relative time difference compared to the lead fin keel was -7, 8, 5 and 5 seconds for the fin, integrated, L- and T-keels respectively. This was for the upwind-downwind course.
- At medium wind speed (12 knots) all keels were practically equal when made in lead or lead/cast iron. The pure iron keels had the following time increases upwind-downwind compared to the lead fin keel: 11, 8, 4 and 4 seconds for the fin, integrated, L- and T-keels respectively.
- In stronger winds (16-20 knots) the bulb keels were better than the fin keels in all materials. The time differences relative to the lead fin keel were -8.0, -8.0 and -8.5 seconds for the integrated, L- and T-keels respectively, in lead averaged over the wind speeds.
- In the new design scenario, with constant Dellenbaugh angle, the fin keel was inferior to the bulb keels for all wind speeds and materials. Averaged over wind speeds the time differences, upwind-downwind, relative to the lead fin keel were -18.3, -18.3 and -20.0 seconds for the integrated, L- and T-keels respectively, made in lead. When designing a new boat the T-keel is thus the best choice from a performance point of view. Negative effects, such as the collection of floating debris and seaweed, differ from area to area and need to be considered as well in the design.
- In practise, the lead/cast iron keel would have been designed for constant displacement, rather than constant shape. That would have given better stability, but could not be achieved here, since the shape was given from the wind-tunnel tests.

7. ACKNOWLEDGEMENTS

The authors would like to express their gratitude to the Department of Applied Mechanics at Chalmers University of Technology for the opportunity to carry out the wind tunnel test in the large wind tunnel.

The financial support from the Rolf Sörman fund for the keel manufacturing is also gratefully acknowledged.

Finally, we would like to thank Björn Axfors and Hanna Tunander for their work in the earlier parts of the project and Stefan Qviberg for originally initiating the project and for his advice in the design of the keels.

8. REFERENCES

1. AXFORS, B. & TUNANDER, H., 2011. *Investigation of Keel Bulbs for Sailing Yachts, Master's thesis*. Chalmers University of Technology, Gothenburg.
2. BARLOW, J.B., WILLIAM, H.R. & POPE, A., 1999. *Low-Speed Wind Tunnel Testing* Third., New York: Wiley-Interscience publication.
3. BÖHM, C. & GRAF, K., 2007. RANSE Calculation of Laminar-to-Turbulent Transition-Flow around Sailing Yacht Appendages. In *Proc. of the 18th Chesapeake Sailing Yacht Symposium*. Chesapeake.
4. LARSSON, L. & ELIASSON, R., 2007. *Principles of Yacht Design* Third., International Marine/McGraw-Hill.
5. LARSSON, L., ELIASSON, R.E. & ORYCH, M., 2014. *Principles of Yacht Design* Fourth., London: Adlard Coles Nautical.
6. LARSSON, L. & RAVEN, H.C., 2010. *Ship Resistance and Flow* J. Randolph Paulling, ed., New Jersey: The Society of Naval Architecture and Marine Engineers.
7. LJUNGQVIST, K. *et al.*, 2012. Investigation of keel bulbs for sailing yachts. In *4th High Performance Yacht Design Conference 2012, HPYD 2012*. Auckland.
8. LURIE, E.A., 2001. On-the-water Measurement of Laminar to Turbulent Boundary Layer Transition on Sailboat Appendages. In *Proc. of the 15th Chesapeake Sailing Yacht Symposium*. Chesapeake.
9. MASKELL, E.C.A., 1963. *Theory of the Blockage Effects on Bluff Bodies and Stalled Wings in a Closed Wind Tunnel*. London: Aeronautical Research Council R&M No 3400.
10. ORYCH, M., RAN, H. & LARSSON, L., 2008. Numerical Investigations Of The Effects Of Winglets On IACC Yacht Drag Components. In *3rd High Performance Yacht Design Conference 2008, HPYD 2008*. Auckland.
11. RANZENBACH, R. & ZAHN, M., 2005. Experimental Methods to Evaluate Underwater Appendages. In *The 17th Chesapeake Sailing Yacht Symposium*. Annapolis, Maryland.
12. RUAG aerospace defence technology, 2004. DNW: DMS–Waage 196–6H Kalibrierbericht zur Version C02.
13. VACANTI, D., 2005. Keel and Rudder Design. *Professional Boatbuilder Issue No 95*, pp.76–97.
14. WERNER, S., 2006. *Computational Hydrodynamics Applied to an America's Cup Class Keel*. Chalmers University of Technology, Gothenburg.
15. WOLFSON UNIT, 2003. WinDesign VPP. Available at: http://www.wumtia.soton.ac.uk/software/windesign-vpp.

THERMAL LOAD EFFECTS ON ALUMINUM LIGHT ALLOY PLATES WITH EPOXY COATINGS

(DOI No: 10.3940/rina.ijsct.2017.b2.206)

D Boote, **T Pais**, **G M Vergassola**, University of Genova, Italy and **D Giannarelli**, Naval Architect, Italy

SUMMARY

When the assembling of hull structure is completed, the sides of metal motor yachts are usually affected by bumps and hollows coming from welding plates to each other and plates to frames. These defects, normally tolerated on merchant ships, cannot be accepted on superyachts for which the external surface must be smooth and glossy. For this reason the surface finishing is achieved by a long and delicate process of filling, fairing and painting.

The final result of this process is very important for the yacht aesthetics as the general appearance of the vessel depends on the external painting. As a matter of fact the quality of painting depends mainly on the undercoat preparation to assure an adequate grip and, most of all, a perfect smooth and faired surface. Despite accurate preparation and painting, surface conditions can undergo undesired alteration because of excessive heating due, as an example, to a long exposure to solar radiation. While stresses do not reach significant values because of the relatively low intensity of thermal loads, strains could still cause very slight surface distortions and undulations which are perceived by human eye as a surface defect. The phenomenon becomes particularly evident if the surface is painted with a dark colour.

In this paper an investigation on the influence of temperature on the stress and strain distribution of aluminium light alloy plates coated by filler layers of different kind and thickness is reported. The study has been performed by FEM structural analyses calibrated by experimental measurements performed on laboratory specimens. This work represents the continuation of a research begun some time ago with the measurement of temperatures on yacht hulls exposed to solar radiation in different conditions.

NOMENCLATURE

λ	Thermal expansion coefficient ($\mu m/m^{-1} K^{-1}$);
ε	Strain tensor;
ε^e	Linear elastic strain;
ε^t	Linear thermal strain;
γ^e	Angular elastic strain;
γ^t	Angular thermal strain;
h_c	Convective coefficient ($W m^{-2} K^{-1}$)
K	Thermal conductivity ($W m^{-1} K^{-1}$)
σ	Stress tensor;
$\boldsymbol{I}$	Unit tensor;
E	Young's Modulus ($N mm^{-2}$);
G	Shear Modulus ($N mm^{-2}$);
ν	Poisson's Ratio;
γ	Density ($t m^{-3}$)
ΔT	Temperature gradient.

1. INTRODUCTION

Without belittling the importance of the huge content of technical aspects, aesthetics and styling for luxury yachts are the most striking characteristics which confer to a pleasure vessel commercial success and honoured position in magazines and reviews for a long time.

Even before external lines and interiors, the quality of painting is, without any doubt, the first aspect that hits the eye of any observer looking at a yacht when entering a marina. The sunlight and the water reflection magnifies the brilliance and glossy nature of yacht sides and superstructures. At the same time the same sunlight and reflection can mercilessly highlight any small defect on the yacht surfaces. For this reason it became mandatory, not only to paint the hull with a maniacal care but, even before, to prepare the surface in a perfect way making it as fair and smooth as possible.

Despite a perfect final result, another aspect can pose a threat to yacht aesthetics: solar radiation. Most yachts spend the majority of time docked in marinas in open air. Based on how the ship is berthed, port and starboard sides may be asymmetrically exposed to solar radiation with a consequent thermal gradient on the hull surface. The extreme consequence of these thermal loads, in the hottest hours of the day, may result in local shell distortion which makes a flat, perfectly bright side an unaesthetic wave sequence; when the temperature decreases the shell returns to be flat and bright. This unpleasant phenomenon mainly depends on two categories of parameters:

- environmental conditions (such as the intensity of solar radiation, the exposure time, the temperatures of the surrounding water and air, the air temperature inside the ship and the effects of wind and waves in dissipating heat);
- structural characteristics of the vessel (such as the hull material, the thickness of shell plates, the structure geometry and residual stresses set up by extremely high temperatures of the welding process during fabrication).

A third, determinant element, which cannot be considered belonging to the first or to the second category, is represented by the colour of the hull paint. In order to study this subject, a joint research programme was started in 2014 by Baglietto Shipyard of La Spezia and the University of Genova, Department of Electrical, Electronic, Telecommunication Engineering and Naval Architecture (DITEN), aimed at investigating the influence of thermal loads on superyacht hull shells. The project has been divided into two phases, starting from the analysis of temperature effects of solar radiation on yacht hulls, up to the evaluation of the interaction between finishing filler and hull plates, both in aluminium light alloys and steel.

Figure 1: An example of welding flaw on the side of a light alloy vessel

Figure 2: Inner view of the structural lay out of a light alloy vessel

The first part of the research has been assessed in detail by Kumar (Kumar, *et al*, 2016); by this study the temperature distribution which can develop on yacht sides of different colours under given environment conditions and exposure times to solar radiation, has been determined. The authors developed a mathematical model able to calculate the temperature on yacht sides and validated it by many real scale measurements by thermal imaging camera.

Starting from the achieved results this paper presents the second part of the research, the aim of which is to predict the stress and strain distribution on the side structures of a light alloy super yacht coated by epoxy filler and dark blue paint exposed to maximum solar radiation.

2. SURFACE PREPARATION

When the construction of the hull structure is completed external plating is normally affected by bumps and hollows, the extension of which depends by the material strength, plate thicknesses and structure lay-out (Figures. 1 and 2). As the designer effort is constantly aimed at reducing the vessel weight the trend is to lower plate thickness, this way amplifying the phenomenon, which becomes further critical in the case of light aluminium alloy vessels.

The defect entity is usually evaluated by measuring the maximum displacement from the ideal surface between two frames by a straight rule. In the case of light alloy vessels built by high level manpower, flaw deepness or protrusions can be limited to a maximum of 6-10 mm with a frame spacing of 1,000 – 1,200 mm (Figure. 3).

To correct these construction defects the usual solution is to coat the complete hull surface with a layer of epoxy filler which is accurately hand smoothed. This is one of the most complicated and time consuming operations of the whole construction procedure which takes many thousands of backbreaking labour hours, carried out parallel to the yacht outfitting. All parts of the hull surface should be made accessible to workers and, in the final phase, painters. This requires that huge scaffoldings should be fitted all around the vessel with walking platforms at various levels in a way that every square centimetre of the hull surface can be properly accessed by workers. The larger is the yacht, the more the difficulties in obtaining a satisfying finish.

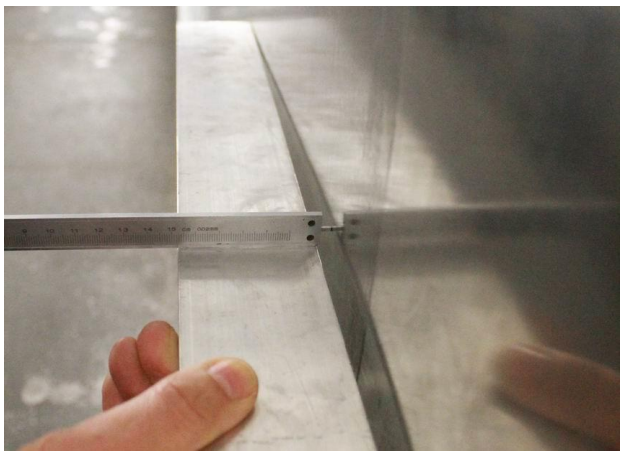

Figure 3: Defect measurement of a light alloy yacht hull between two frames

When all the preparation work is carried out the hull is ready to be painted. Painting is carried out in a strictly controlled shed environment, where temperature,

humidity and air quality should comply with very strict limit conditions. Then a first layer of "show coat" paint, usually of a dark colour, is applied to highlight flaws, irregularities, and other potential problematic areas. Hull painting, with the definitive colour, closes this binding, expensive and time consuming operation but, when the superyacht sparkles into the water, shipyard and owner agree the final result well worth the effort.

Despite this painstaking preparation and accurate painting, sometimes surface conditions can undergo undesired alteration because of excessive heating due, as an example, to a long exposure to solar radiation. This can cause very slight surface distortions and undulations which, by human eyes, are perceived as surface defects. The phenomenon could become particularly critical when the hull is painted with dark colours because of their attitude to accumulate more heat and reach higher temperatures.

For this reason the classic colour of the conventional yacht fleet is thus, unsurprisingly, white. White paints are cheaper, better at hiding imperfections, and do not glitter and reflect as much as dark paints, which show dirt, salt splashes and other defects quite easily. Moreover, white neither fades as fast as other colours, nor does it need as much maintenance.

Nevertheless, recent trends see owners opting for darker colours such as black or blue, which absorb much more solar heat, often resulting in deformations that invalidate the aesthetics of the yacht. Reasonable solutions to avoid such unpleasant surprises could be stronger scantlings and more expensive hull coatings, besides powerful ship cooling systems. Unfortunately, these expedients dramatically increase the vessel's weight and cost.

In order to collect reliable information about the influence of dark colours on the plate deformation of a hull structure caused by thermal loads, the present research has been started based on thermo-structural analysis of a typical hull structure of an aluminium light alloy superyacht.

3. THERMO-STRUCTURAL ANALYSIS

Stress and strains are not always caused by forces and/or moments; typically an homogeneous body, free from constraints and subject to a continuous temperature variation, undergoes thermal deformation without any stress arising.

In complex structures with constrained components, such as a hull structure, thermal deformations come together with other linear and angular deformations which can be evaluated by the following relationships (the index k and l identify each component of linear and angular deformation in x, y and z direction):

$$\varepsilon_k = \varepsilon_k^e + \varepsilon_k^t \qquad \gamma_{kl} = \gamma_{kl}^e + \gamma_{kl}^t \tag{1}$$

where:
^{e} = linear elastic strain;
ε^t = linear thermal strain;
γ^e = angular elastic strain;
γ^t = angular thermal strain.

In isotropic materials elastic deformations (superscript *e*) are related to stress distribution. Temperature gradients ΔT do not produce any angular deformation; thermal deformations (superscript *t*) have only the linear component ε, the same in each direction *x* and *y* and related to ΔT through the coefficient of thermal expansion λ of the material, which defines the deformation resulting from a unit temperature variation. The linear and angular thermal contribution can then be written as:

$$\varepsilon_x^t = \varepsilon_y^t = \varepsilon_z^t = \lambda \Delta T \qquad \gamma_{xy}^t = \gamma_{yz}^t = \gamma_{zx}^t = 0 \tag{2}$$

In the xy plane:

$$\varepsilon_x = \frac{1}{E}(\sigma_x - \nu\sigma_x - \nu\sigma_z) + \lambda\Delta T \qquad \gamma_{xy} = \frac{1}{G}\tau_{xy} \tag{3}$$

From the previous equations, the Hooke-Duhamel relationship can be written:

$$\varepsilon = \frac{1+\nu}{E}\sigma - \frac{\nu}{E} trace(\sigma)\boldsymbol{I} + \lambda\Delta T\boldsymbol{I} \tag{4}$$

where:

σ = stress tensor;
ε = strain tensor;
$\boldsymbol{I}$ = unit tensor;
E, ν = elastic constants;
λ = thermal expansion coefficient of the material;
ΔT = temperature gradient.

The stress and strain distribution on the hull side plates caused by solar radiation can be evaluated by a thermo-structural analysis carried out through three subsequent stages:

- thermal analysis, by which the temperature distribution can be determined under given initial conditions;
- transfer of the temperature distribution to the structural model as "load conditions";
- thermo-structural analysis, by which the displacements and stress distribution can be calculated.

Thermal loads are generally given under the form of heat flows induced in a body by the exposure to a radiation source by conduction, convection or irradiation mechanism; thermal constraints are represented by specified temperatures in some areas, while the conduction, convective and irradiation exchange coefficients complete the definition of the boundary conditions.

Once the mathematical model of the body is set up, the thermal analysis allows to calculate the temperature distribution in each point of the system, by applying to the model the equations of heat transfer by conduction, convection and radiation.

Thermal analysis can be performed in a steady state (stationary thermal analysis) or as thermal transient, studying the progress of the thermal variables as a function of time until a stable equilibrium of the system is reached. Typically the thermal analysis is non-linear because heat transfer coefficients in turn depend on the temperature.

Once the temperature distribution is known, it should be mapped to the numerical model used for structural analysis as "load condition". This operation may be trivial if the same computational mesh is to be used for both thermal and structural analysis, otherwise a spatial interpolation will be necessary.

4. LABORATORY TESTS

Before the structural analysis of the yacht structures, an experimental activity has been carried out in order to find proper parameter values to be introduced in the FEM calculations. This activity has been performed in cooperation with Boero Bartolomeo S.p.A., one of the largest and oldest Italian producers of paints and fillers involved in the yacht field.

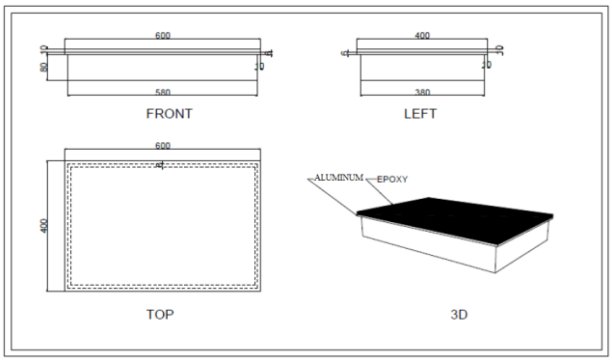

Figure 4: Geometric characteristics of the specimen.

The base specimen, specifically built for this research, used aluminium light alloy (L.A.) plate welded to an orthogonal frame simulating a side panel stiffened by longitudinals and frames (Figures. 4 to 6); an AlMg5083 L.A. has been used. In total four specimens have been prepared and on each of them the initial distortion at the panel centre due to welding operation has been accurately measured in the Boero laboratory and synthetically reported in Table I. In two cases the deformation resulted to be towards the bottom (convex) and only in one case (specimen n.1) towards the top (concave); in one case the plate resulted to remain flat (specimen n.4).

Figure 5: L.A. specimen n.1: top view

Figure 6: L.A. specimen n.1: particular of intermitting welding.

The plates have been coated with a layer of standard Epoxy filler, 10 mm thick, normally used on superyacht finishing operations (see Figure. 7). The main characteristics of the light alloy and filler used on the specimens are resumed in Table II.

Table I: Initial deformation of light alloy specimens

Specimen	Initial displacement – Light alloy	
	Curvature	Displ [μm]
n. 1 – 6 mm	Concave	1,300
n. 2 – 6 mm	Convex	200
n. 3 – 6 mm	Convex	450
n. 4 - 5 mm	Plane	0

Figure 7: L.A. specimen n.1: plate with filler coating

Table II: Main characteristics L.A. and filler

Item	Aluminium "AlMg 5083 H321"	Filler "A"	Filler "B"
E [N/mm^2]	70,000	1,500	1,200
ν	0.33	0.40	0.40
G [N/mm^2]	26,000	535	402
γ [t/m^3]	2.70	0.7	0.7
Thermal expansion coefficient λ [µm/m°K] (35-40°C)	24	61	71
Thermal expansion coefficient λ [µm/m°K] (80-100°C)	24	84	99
Λ [µm/m°K]	24	50	50
K [W/m°C]	24	0.13	0.13

The temperature developed by the filler during the polymerization process has been measured, resulting to be in a range between 30 °C and 35 °C. Then the filler has been heated by exposing its surface to an infrared lamp, simulating the solar radiation. After an exposure of 50 minutes, on each specimen the following quantities have been measured and synthetically reported in Table III:

- filler and L.A. temperatures;
- thermal conductivity *K*;
- thermal expansion coefficient λ;
- plate and filler displacement at centre point.

Table III: Measurement results on L.A. specimens.

Spec	T filler	T L.A. plate	*K* [W/m °K]	λ [µm/ m°K]	Displ filler [µm]	Displ plate [µm]
1	65.0	46.0	0.13	50/65	-	322
2	61.5	41.0	0.13	90	756	805
3	61.3	39.5	0.14	50	364	383
4	64.8	43.0	0.14	50	658	674

A numerical model reproducing the same specimen has been set for FEM analysis by the multipurpose NASTRAN-PATRAN code (MSC Software Corporation, 2014). The model has been built by 8 nodes, HEX-8, solid element of NASTRAN library. The choice of solid elements was justified by the fact that, in thermal analysis, both stress and strain are expected to be very little, as confirmed by the previous experimental investigation. For this reason the model should take into account all kind of stresses, and a shell element model should not be allowed to have the necessary precision neglecting the torsion contribution.

For each specimen the model geometry has been set up by reproducing the deformed pattern resulting from welding operations and synthesised in Table I.

The model consisted of HEX-8 elements with a maximum dimension of 5 and 6 mm, according to the real specimen. In this way the total thickness of L.A. plates has been realised by one element, while the filler has been reproduced by two elements (Figure. 8).

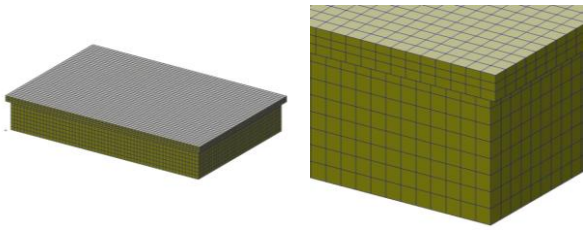

Figure 8: Nastran numerical model of the specimen.

4.1 THERMAL ANALYSIS

On the FE model a non linear thermal analysis (SOL 153 in Nastran library) has been set up by imposing the following boundary conditions:

- Initial model temperature: on all nodes of the model a uniform temperature of 22°C has been imposed;
- Final epoxy temperature: the measured temperatures on the epoxy top surface after an exposure of 50 min to an infrared lamp are reported in Table III; these have been used as final values;
- Convection heat transfer coefficient h_c: this coefficient represents the thermal power exchanged between a solid surface and a fluid in relative motion, per unit area and per unit of temperature difference. For the laboratory tests a value of h_c equal to 9 W/m^{2}K have been assumed to correctly simulate natural convection conditions of the laboratory;
- Thermal conductivity *K*: thermal conductivity represents the ability of a material to transmit heat (i.e. the greater the value of *K*, the less the insulating capability). Its value depends only on the nature of the material, not by its shape. For the materials used in the laboratory tests a value of *K* = 24 W/m°C for L.A. and *K* = 0.13 W/m°C for epoxy have been assumed (see also Table II).

The achieved results can be seen in detail in the plots of Figure. 9 and 10 where the temperature gradient through the plate (epoxy + L.A.) are clearly shown. The temperature on the epoxy top surface remains the initial one, equal in this case to 64.7°C; the temperature on the bottom L.A. plate has dropped to 33 – 34°C.

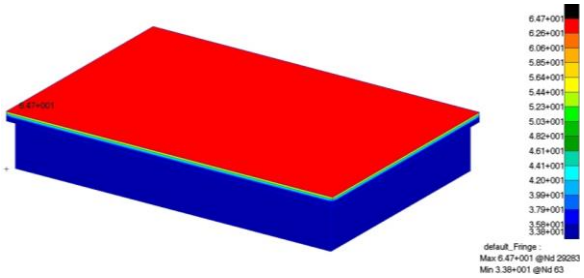

Figure 9: Thermal analysis results on specimen n.1.

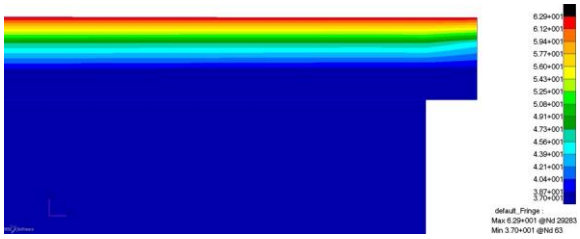

Figure 10: Temperature gradients through epoxy layer and L.A. plate.

4.2 STRUCTURAL ANALYSIS

The temperature distribution resulting from the thermal analysis has been transferred to the FEM structural model point by point to create the correspondent "temperature field". The model has been simply supported on the lower edge of the reinforcements and the thermal expansion coefficients λ of the two materials assigned according to the values reported in Table II. In Figure. 11, as an example, the vertical displacements obtained for specimen n. 1 are shown.

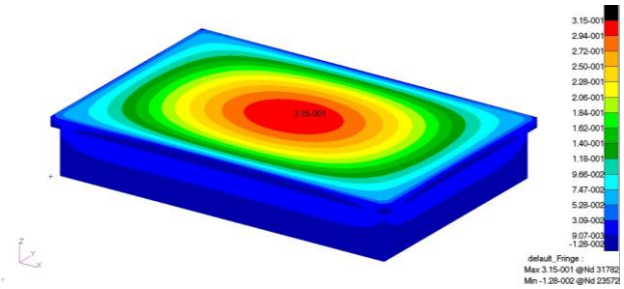

Figure 11: Vertical displacements of specimen n.1.

Both thermal and structural analyses have been carried out for all the four specimens and for each of them the maximum displacement at the plate centre has been recorded and compared with that measured on the real structures during laboratory tests; the resulting values are synthesised in Table IV.

Table IV: Comparison between measured and FEM displacements.

Spec.	Boero		FEM		Error filler %	Error plate %
	Displ filler [µm]	Displ plate [µm]	Displ filler [µm]	Displ plate [µm]		
1	-	322	333	319	-	-0.9
2	756	805	803	771	5.9	-4.4
3	364	383	338	326	-7.7	-17.5
4	658	674	651	631	-1,1	-6.8

5. HULL FE MODELING

For the current investigation a 46 meters light alloy superyacht has been assumed as a study case. The hull has a longitudinal type structure with longitudinal stiffeners at 300 mm each other supported by reinforced frames with 1,070 mm spacing. The side plating of the hull is coated by a layer of epoxy filler which hides welding toes, imperfections of any kind and allows to get a perfectly smooth surface.

Starting from the technical drawings of the vessel, kindly provided by the shipyard, a 3D model of a portion of the hull structure between two structural bulkheads has been carried out by Rhinoceros software (Mc Neel & Associates, 2013). The hull slice has a length of about 6.5 meters. Working on the Rhinoceros model the FEM numerical model has been obtained. Also in this case the MSC Nastran/Patran code has been used. In order to obtain a numerical model as close as possible to the real structure it was decided to use 3D, 8 nodes HEX-8 solid elements for the side shell: aluminium plates and epoxy filler have been modelled by one layer of solid elements. Deck and bottom structures and transverse frames have been modelled by 4 nodes QUAD-4 shell elements, while for stiffeners 2 nodes BEAM-2 have been utilised. Aluminium light alloy and epoxy filler have been modelled according to the characteristics listed in Table II.

Only one half of the hull portion has been modelled and constrained by symmetry boundary conditions. The resulting model, shown in Figure. 12, consists of 35,500 nodes and 30,800 elements. In Figure. 13 a particular of the side shell with HEX 8 elements is shown as well.

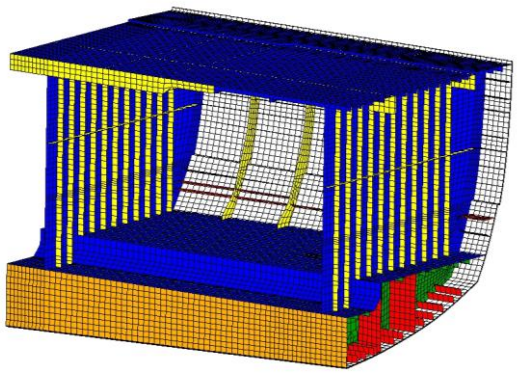

Figure 12: Finite element model of the hull portion.

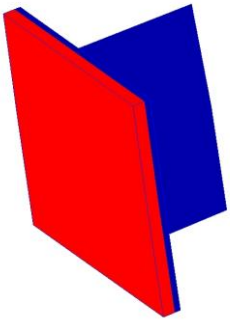

Figure 13: Particular of side shell FE model: two layers of solid elements have been used for epoxy filler (in red) and aluminium light alloy plates (in blue).

6. THERMAL ANALYSIS

6.1 BOUNDARY CONDITIONS

Once the FE model has been completed the thermal analysis has been prepared on the base of well known principles contained in (Cengel, 2015), (Zienkiewicz *et al*, 2005) and (Reddy and Gartling, 2010). The FE model has been set up by applying the following boundary conditions:

- Initial model temperature: on all nodes of the model a uniform external temperature of 24°C has been imposed;
- Outside epoxy temperature: as shown in the thermal image taken from the work of Kumar *et al* (2016), shown in Figure 14, the temperature curve experiences an increase from the floating plane up to the sheerstrake (Figure. 15). Since the numerical model represents a hull portion between section "C" and "E" in Figure 14, the temperature curve D has been applied to the external epoxy coat. The exact trend is shown in Figure. 16 where it is possible to see that the temperature is constant and equal to 24°C up to the water line, and then it grows approximately linearly up to the maximum temperature of 55°C.

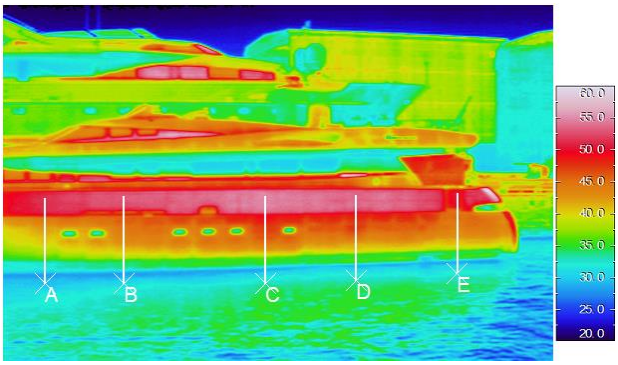

Figure 14: Temperature measurement by thermal imaging camera on 5 hull sections.

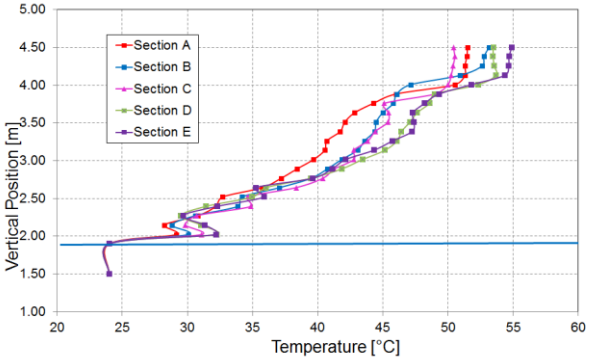

Figure 15: Temperature growth from floating line to the bulwark along 5 hull sections A, B, C, D and E.

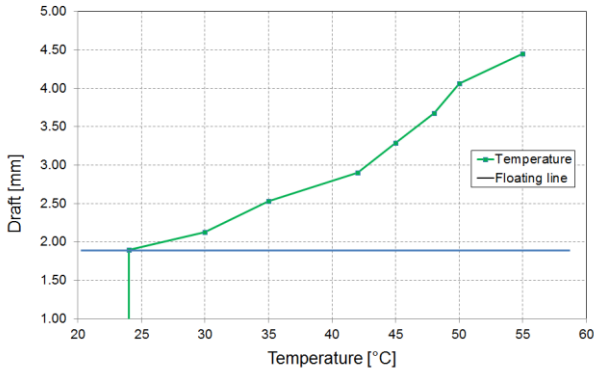

Figure 16: Temperature distribution applied to the side shell in thermal calculations.

- Convection heat transfer coefficient h_c: for current FE thermal calculations variable values of h_c have been assumed to correctly simulate natural convection conditions in water and in air.
  - h_c = 1,000 W/m^2 K for element faces located below the water plane;
  - h_c = 10 W/m^2 K for element faces in contact with air, inside the hull (the internal temperature of the yacht was assumed equal to 22°C);
  - h_c = 25 W/m^2 K for elements faces in contact with air, external (this because the external faces are exposed to atmospheric agents, such as wind, which increase the heat exchange between surfaces and air).
- Thermal conductivity *K*: For materials used in thermal analyses, aluminium light alloy and epoxy filler, the assumed values are those listed in Table IV.

6.2 THERMAL ANALYSIS RESULTS

Starting from initial temperature conditions, the SOL 153 Nastran routine increases the temperature up to the maximum final value, set on the epoxy filler nodes (55°C), and calculates the heat flux and heat transfer corresponding to the previously described coefficients. The final result is a refined map of temperature on all

layers of the model: epoxy, aluminium, internal and external, plates and frames.

In Figures. 17 and 18 two synthetic plots of thermal analysis results are shown for the outer surface of the hull (epoxy) and the internal part of the hull (aluminium structures) respectively. The first plot simply reflects the temperature distribution imposed on the epoxy external surface (see Figure. 16).

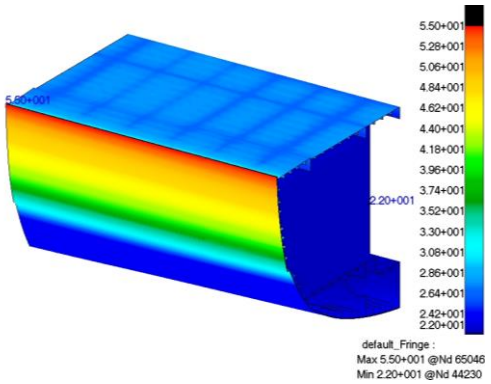

Figure 17: Temperature distribution on outer surface.

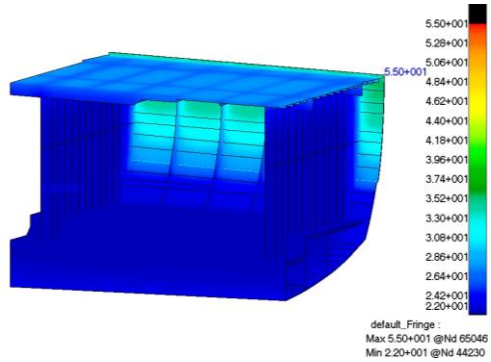

Figure 18: Temperature distribution on inner side.

What comes out from this analysis is the temperature variation through the plate thickness, from the epoxy external surface to the inner aluminium plates. As Figure. 19 clearly shows the epoxy is a highly insulating material that, through its 10 mm thickness, lowers the temperature of some 20 degrees. On the other side, aluminium is a good heat conductor and, as a consequence, the temperature gradient through its thickness is practically equal to zero.

In addition aluminium plates transfer heat to inner structures to which it is welded, further lowering its heat content and temperature. The next Figure. 20 shows very clearly the heat conduction from the aluminium shell (about 35°C) to internal side frames (about 28°C) which efficiently work as heat dissipaters. On the bottom, close to the floating water line, the temperature remains fixed at the initial value of 24°C.

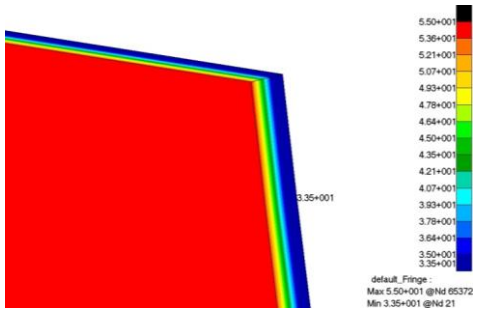

Figure 19: Temperature gradient through the plate thickness.

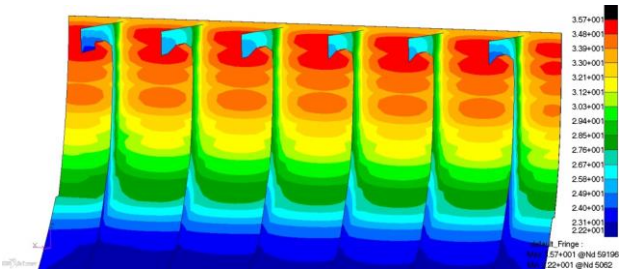

Figure 20: Temperature distribution on internal structures.

7. STRUCTURAL ANALYSIS

As the final step, structural analysis has been set up; having at disposal the temperature distribution gathered by the previous thermal analysis and being the thermal FE model identical to the structural one, temperatures have been easily transferred to the structural model point by point, thus creating the correspondent "temperature field".

Then, since the structural analysis has to be run on a hull portion, it has been necessary to restore the continuity with the rest of hull structure by applying appropriate boundary conditions. The model has been constrained at its extremities in correspondence of bulkheads and symmetry conditions have been applied on the central plane.

In this part of the investigation, as already done for thermal analysis, a geometric perfect model of the vessel has been considered, that is to say a model without defects and imperfections coming from welding or other construction procedures.

For what the mechanical properties of materials are concerned, when carrying out a thermo-structural analysis, besides usual properties such as the elastic modulus, shear modulus and Poisson's ratio, thermal expansion coefficients λ of materials have to be defined. This coefficient is a measure of the capacity of thermal expansion of a body and, while for aluminium its value doesn't depend on temperature, in the case of epoxy filler, being a polymeric material, it varies significantly with the temperature. More precisely λ undergoes a

considerable increase in passing from the "glass state" (below the "glass temperature" T_g) into the "plastic state" (above the T_g). For this kind of epoxy the T_g falls exactly in the range of temperatures we are interested in, say 30-60°C, with the plastic transformation taking place at around 35-40°C.

For this reason, as shown in Table II, two λ fields have been fixed, 35-40°C and 80-100°C, and within these two ranges a linear law of variation for λ has been assumed for FE calculations. Once all the thermal and mechanical parameters have been correctly set up, a series of different models have been prepared by varying the aluminium plate thickness and the filler type. A constant value of 10 mm for the filler thickness has been assumed for all models, listed in the following Table V. In the case of A model, with the thinnest plates, an additional case has been considered, by adding to the structure vertical bars at stiffener mid span. This solution was taken into consideration to compare it with C and D thicker models. Finally, a specific model coated with a different kind of epoxy filler, named "B", has been considered.

Table V: FEM models.

Model	Al thickness [mm]	Filler type	Filler thick [mm]
Model A	5	A	10
Model A + Bars	5	A	10
Model B	5	B	10
Model C	6	A	10
Model D	7	A	10

7.1 ANALYSIS OF RESULTS

FE calculations have been run on all models and for each of them detailed results have been extracted and evaluated. In this paper, for space reasons, only the most significant ones are shown. In Figure. 21, as an example, the deformed configuration of model "A" is reported; being this the model with thinnest plates, the side deflections between fixed bulkheads are the largest ones.

Owing to the structural lay out of this yacht, two main zones have been individuated with different behaviours: the central side, zone (a) and the upper side strip, the sheerstrake, zone (b). On each area two orders of displacements can be individuated: a first more evident order of deformation on the whole side (a), with the maximum value at mid distance between bulkheads, at distance L_B, and a second order deformation between two consecutive frames, at distance L_F, on the sheerstrake (b).

In the (b) zone the first order deformation is reduced because of the stiffer sheerstrake structure, making more evident the second order displacements between frames. This is what makes the "undulation" effects of the painted surface more evident.

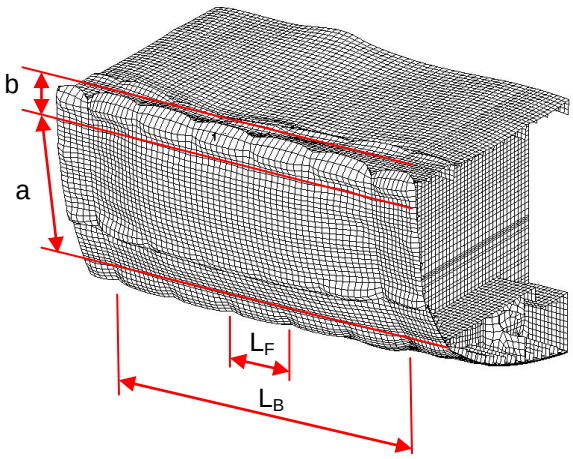

Figure 21: Model A: deformed pattern.

To give a quantitative idea of side deformations, Figure. 22 shows the intensity of displacement resultants in three directions. The deformation perpendicular to the side surface is the sum of the epoxy filler expansion and of the aluminium plate displacement.

This figure clearly shows how, especially in the upper part of the structure (the warmest area of the model), deformations reach their maximum values at the centre of the plate between two transversal reinforced frames.

As the epoxy filler has a thermal expansion coefficient three to four times that of aluminium, when it warms up it expands and pushes/pulls the aluminium plates to deform. The maximum displacement is then the sum of epoxy expansion and aluminium deflection. In this case, as an example, the total deflection reaches a value of 1,250 μm (slightly more than 1 mm) perpendicular to the side surface.

Epoxy and alloy displacements have been determined with respect to the undeformed surface (initial side geometry) along an element strip of zone (a), path line 1, and along an element strip of zone (b), path line 2, as shown in Figure. 22. In Figure. 23a the strip shape shows that the whole side in zone (a) warps bending outside in a unique, continuous wave of length L_B.

In Figure. 23b displacements are reported in a diagram with a blue curve for aluminium and a red one for epoxy. On the top ruler the bulkhead and frame positions are shown. Markers represent the nodes in correspondence of frames and those at mid span of panels between frames. As it is possible to see the curve trend doesn't show any "wave" effect, that is, there are not big differences between displacements in correspondence of frames and on the panel centre.

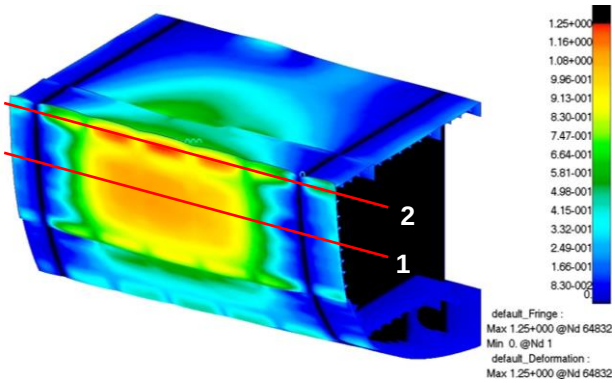

Figure 22: Model A: displacement plot

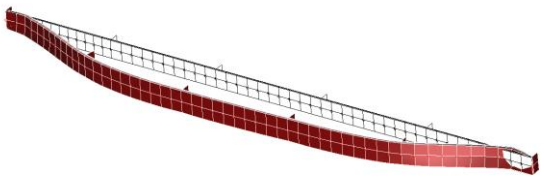

Figure 23a: Element strip of zone (a), path 1: deformation plot of model A.

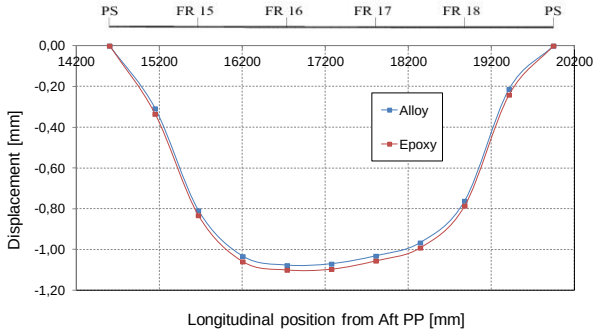

Figure 23b: Zone (a), path 1: alloy and epoxy displacement curves for model A.

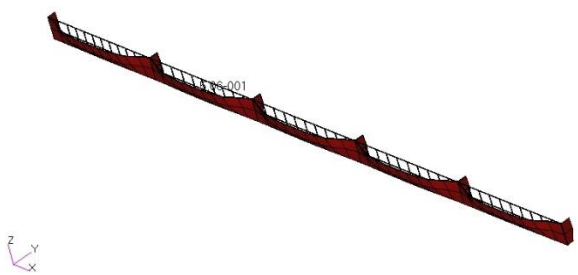

Figure 24a: Element strip of zone (b), path 2: deformation plot of model A.

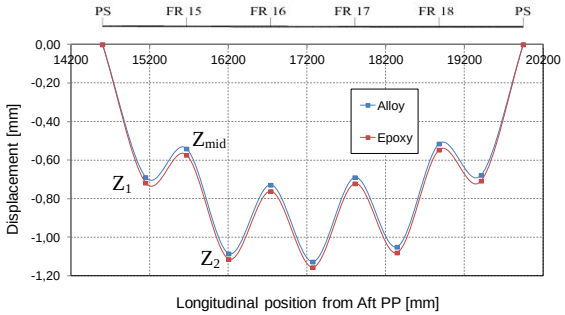

Figure 24b: Zone (b), path 2: alloy and epoxy displacement curves for model A.

With the same approach, displacements of the element strip of path 2, in correspondence of the sheerstrake, are qualitatively shown in Figure. 24a and quantitatively reported in the diagram of Figure. 24b. Again the blue curve refers to aluminium plate surface, while the red one represents epoxy filler external surface.

On path 2 a significant difference comes out between displacements of nodes in correspondence of frames and those at mid span of panels between frames. This difference, which can be defined as the "wave amplitude" of the surface defect, can be simply quantified by the relationship:

$$\Delta z = z_{mid} - \frac{z_1 + z_2}{2} \qquad (5)$$

Depending on its value, the wave amplitude Δz, can give to the observer a "wave-shaped" view of the side which is perceived as an unpleasant side defect. For model A the difference is about 350 μm, enough to give to the side surface a visible undulating shape.

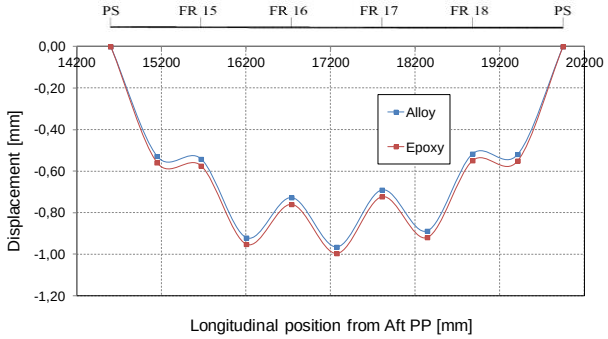

Figure 25: Zone (b), path 2: alloy and epoxy displacement curves for model D.

The same trend previously presented for model A recurs for other models with higher thickness, the only difference being smaller deflections. The graph in Figure. 25 shows model D behaviour in correspondence of line path 2; in this case aluminium plates have a 7 mm thickness which reduces the "wave amplitude" to less than 200 μm and giving to the side a more smooth, flat appearence.

In the last examined case, model A has been modified by adding vertical reinforcements at mid span of all shell panels, between longitudinals, as schematically represented in Figure. 26 by white bars. In this scenario the original 1,000x300 mm plate has been halved in two, 500x300 mm. As it is possible to see in the deformation plot of Figure. 27a, on the sheerstrake it's clearly visible how side plates warp between frames and bars, instead of on the entire panel span from frame to frame, thus reducing the displacement. In Figure. 27b the comparison of sheerstrake displacements of model A and A+bars is shown.

As for previous cases, alloy and epoxy nodal displacements have been plotted on the diagram shown in Figure. 28. The effects of bars seems to get very good results for what displacements values are concerned: maximum values are much lower than those resulting from model A.

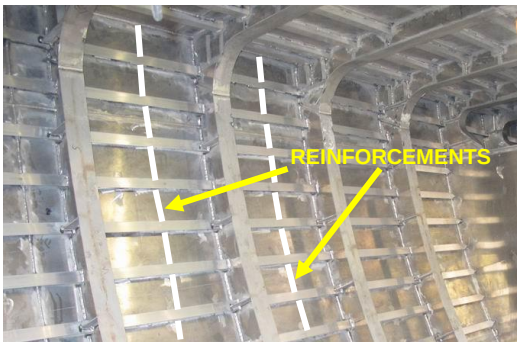

Figure 26: Inside view of the real structure of the superyacht under study with vertical reinforcements.

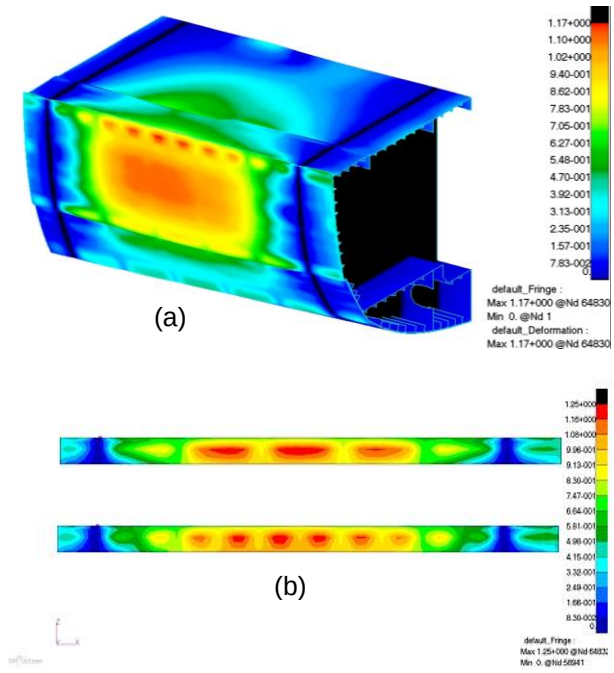

Figure 27: (a) displacement plot of model A+bars; (b) comparison between zone (b) displacements of model A and model A+bars.

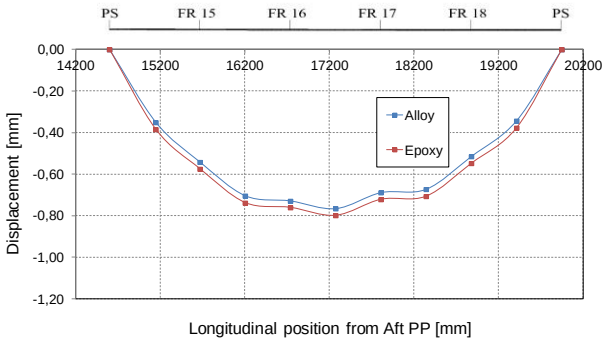

Figure 28: Zone (b), path 2: alloy and epoxy displacement curves for model A+bars.

For all models the average of all the wave amplitudes Δz of each path line have been calculated and reported in the following Table VI.

Table VI: Maximum displacements

		Max wave amplitude of the surface defect	
Model	Material	Path line 1 Average Δz [μm]	Path line 2 Average Δz [μm]
Model A	Alloy	91	451
	Epoxy	93	447
Model A + Bars	Alloy	#	86
	Epoxy	#	103
Model B	Alloy	102	656
	Epoxy	105	649
Model C	Alloy	95	356
	Epoxy	96	354
Model D	Alloy	97	286
	Epoxy	98	285

8. CONCLUSIONS

In this paper an investigation on the influence of temperature induced by solar radiation on the mechanical behaviour of aluminium light alloy plates coated by filler layers of different kind and thickness is presented. The research has been carried out in cooperation between Baglietto Shipyards and the University of Genova, Department of Electrical, Electronic, Telecommunication Engineering and Naval Architecture (DITEN).

The study has been performed by FEM structural analyses calibrated by experimental measurements performed on specimens realized in the Boero Bartolomeo S.p.A laboratories. This work represents the continuation of a previous research on the measurement of temperatures on yacht hulls exposed to sun radiation in different conditions.

As stresses are not significant for what the material resistance is concerned, strains can produce plates

distortions which, over certain values, becomes visible at human eye giving an unpleasant effect of "side undulation".

The future developments of this work, underway at present, consist in determining the maximum Δz value for which the undulation effect is not perceptible by human eye, giving to the side surface a perfect smooth and planar aspect. Then steel yachts should be investigated as well; in this respect another series of steel panels will be realized and examined by laboratory tests in order to validate the thermal and structural FEM calculations. Finally, the real geometry of the structure shall be modelled taking into consideration welding defects mapped by previous measurements carried out during the vessel construction.

9. ACKNOWLEDGEMENT

The authors wish to thank Mr. R. Ricotti for his precious contribution on the panel characterization in the Boero Bartolomeo S.p.A. laboratory.

10. REFERENCES

1. KUMAR V., BOOTE D., PAIS T., PENCO G., "*Development of a Parametric Model for Analysing Temperature Effects of Solar Radiation on Yachts*" RINA Transactions of the Royal Institution of Naval Architects Part B: International Journal of Small Craft Technology, Volume 158, pp. B1-B13 (UK), 2016.
2. MSC SOFTWARE CORPORATION, "*Nastran User Guide*", Newport Beach, CA, USA, 2014.
3. MC NEEL & ASSOCIATES, "*Rhinoceros 5 User Guide*", Seattle, WA, USA, 2013.
4. CENGEL Y.A., "Heat and Mass Transfer", Mc Graw Hill, New York, USA, 2015.
5. ZIENKIEWICZ O.C, TAYLOR R.L, ZHU J.Z, "*The Finite Element Method for Solid & Structural Mechanics*", Elsevier, Amsterdam, 2005.
6. REDDY J.N., GARTLING D.K., "*The Finite Element Method in Heat Transfer and Fluid Dynamics*", Taylor & Francis Group, Boca Raton, 2010.

The Transactions of The Royal Institution of Naval Architects – Part B

International Journal of Small Craft Technology

GUIDANCE NOTES FOR AUTHORS

All papers, technical notes and discussions should be submitted in electronic form, normally in MSWord format. Authors wishing to submit in other formats should first contact RINA Headquarters. Submissions should be forwarded on PC compatible disks or CD-ROM, containing the full text, including inserted figures. Submissions less than 5Mb may be forwarded by email or online.

Authors are responsible for obtaining security clearance as required. If they so wish, authors may add a disclaimer stating that the opinions expressed are solely those of the author.

In submitting papers or technical notes for publication, authors implicitly assign copyright to the Royal Institution of Naval Architects if the paper or technical note is published. Where copyright is held elsewhere, authors must present evidence of approval to re-publish.

When submitting contributions for publication, authors must state if the paper or technical note has been published before and where, or whether it is being considered for publication by some other publisher

Papers: Papers should not normally exceed 6000 words (with up to 10 illustrations). Longer papers where the content justifies the extra length may be published at the Editor's discretion. The required format of papers submitted for publication may be obtained from the RINA website or from RINA Headquarters

Technical Notes: Technical notes should not normally exceed 1500 words (and up to 5 illustrations). The required format of technical notes submitted for publication may be obtained from the RINA website or from RINA Headquarters

Discussion: Discussion of published papers, or comment on published discussion, should not normally exceed 500 words (with up to 2 illustrations).

All submissions for publication should be forwarded to:

The Editor (IJSCT)
The Royal Institution of Naval Architects
8-9 Northumberland Street
London WC2N 5DA, UK
Tel: +44 (0)20 7235 4622 Fax: +44 (0)20 7259 5912
Email: ijsct@rina.org.uk Online: www.rina.org.uk

THE ROYAL INSTITUTION OF NAVAL ARCHITECTS

The Royal Institution of Naval Architects is an internationally renowned professional institution and learned society, whose members are involved at all levels in the design, construction and repair of ships, boats and maritime structures, in over 80 countries. RINA is widely represented in the marine industry, universities and colleges, and maritime organisations worldwide.

Membership is open to those who are professionally qualified in naval architecture or a related subject, or who are involved or interested in the maritime industry. RINA members enjoy a wide range of benefits and services, including advice on education, training and professional development. The RINA also publishes a range of technical journals, books and papers, and organises an extensive programme of international conferences and training courses covering all aspects of naval architecture and maritime technology, available to members free or at reduced rates

The Transactions of The Royal Institution of Naval Architects

Vol 159 Part B2 2017 ISSN 1740-0694

International Journal of Small Craft Technology

CONTENTS

PAPERS

TECHNICAL NOTES

There are no Technical Notes published in this issue of the IJSCT

DISCUSSION

There are no Discussions published in this issue of the IJSCT